TUDelft

Delft University of Technology

Advances in Aerosol Instrumentation for Atmospheric Science

Barmpounis, K.

DOI

10.4233/uuid:5594067b-1646-46b1-a3d0-95aec9f5af7a

Publication date
2020

Document Version
Final published version

Citation (APA)
Barmpounis, K. (2020). *Advances in Aerosol Instrumentation for Atmospheric Science*. [Dissertation (TU Delft), Delft University of Technology]. https://doi.org/10.4233/uuid:5594067b-1646-46b1-a3d0-95aec9f5af7a

Important note
To cite this publication, please use the final published version (if applicable).
Please check the document version above.

Advances in Aerosol Instrumentation for

Atmospheric Science

Dissertation

for the purpose of obtaining the degree of doctor
at Delft University of Technology
by the authority of the Rector Magnificus Prof.dr.ir. T.H.J.J. van der Hagen
chair of the Board for Doctorates
to be defended publicly on
Monday 9 November 2020 at 10:00 o'clock

by

Konstantinos BARMPOUNIS
Master of Environmental and Ecological Engineering, University of the Aegean, Greece
born in Karditsa, Greece

This dissertation has been approved by the promotors.

Composition of the doctoral committee:

Rector Magnificus, chairperson

Prof. Dr.Andreas Schmidt-Ott Delft University of Technology, promotor

Prof. George Biskos Delft University of Technology, promotor

Independent members:

Prof. Knut Deppert Lund University, Sweden

Prof. Dr. Paul Winkler University of Vienna, Austria

Prof. Athanasios Konstantopoulos University of Thessaloniki, Greece

Prof. Ruud van Ommen Delft University of Technology

Other members:

Prof. Michel Attoui UPEC Sciences, France

Table of Contents

Introduction

The earth's atmosphere is a multivariate dynamic system, with complex interactions and hard to predict outputs. Climate is a major parameter that affects agriculture, human habitats and influences the economy of countries, to mention just a few. In addition, pollution levels of the lower part of the atmosphere is strongly correlated with human health effects.(Kampa and Castanas 2008; Pöschl 2005). Air pollution is a major problem in many cities around the world. The work described in this thesis aims in answering open questions in the field of atmospheric physics and provide experimental tools with which future research can be performed more efficiently.

In a first oversimplified approach, the atmosphere is a vast chemical reactor which contains gases and solid matter in the form of particles, powered by solar radiation and stirred by the combined influence of the Earth's rotation and pressure/temperature differentials. Particles provide the necessary surface on which water vapors condense and form clouds. The role of clouds in the atmosphere is very important. They form a protective blanket from solar radiation, but also provide the closing link in the water balance between water masses and atmosphere. Without clouds and rainfall, water would not find its way back to land. Furthermore, particles in the atmosphere is contribute to the radiative forcing of the atmosphere by directly absorbing or reflecting solar radiation.

The uncertainties, regarding the contribution of particles, are large and this is mainly attributed to the large diversity of particles with different properties. Given that the interaction of light with particles is a function of the particle properties, it is hard to conclude on whether particles are cooling or warming the atmosphere. For example, black carbon particles absorb radiation, resulting in warming of the atmosphere (Jacobson 2001) meanwhile sulphates scatter radiation resulting in cooling of the atmosphere. Concluding on which direction the sum of all the contributions goes to, is not a straightforward task. To this day, the effect that particles have in the atmosphere remains one of the biggest unknown parameters in understanding climate change (IPCC, 2014).

What is required to come to a better understanding of the role of particles in the atmosphere? First, it is necessary to identify the sources of particles in the atmosphere. Particles originate from a big variety of anthropogenic and natural sources. Natural sources of particles include volcanic eruptions, sea spray and wildfires. These are sources, which, although very

localized, contribute significantly to the number of particles released in the atmosphere (Viana et al., 2014).

An important natural mechanism through which particles are formed is via nucleation and/or condensation of gaseous species present in the atmosphere. This mechanism is generally referred to as new particle formation (NPF). Studies suggest that a significant fraction of the global budget of cloud condensation nuclei originates from NPF processes.(Kulmala et al. 2013; Rose et al. 2017) In principle, NPF starts with the formation of clusters having sub-1 nm sizes, which grow through simultaneous nucleation and coagulation processes. Proposed mechanisms of NPF include interaction of sulphuric acid with volatile organic compounds, binary nucleation, and ion-induced nucleation.(Schobesberger et al. 2013) The importance of investigating and understanding NPF derives from a vast number of field observations which confirm that NFP is a frequent global phenomenon.

The formation of a large number of new particles in the atmosphere has been observed worldwide at various rural, marine and urban sites, highlighting that NPF constitutes a significant source of atmospheric aerosol particles.(de España et al. 2017; Kulmala et al. 2004; Kulmala et al. 2013; Platis et al. 2016) The identification of the initiating mechanism of NPF, however, remains one of the most interesting questions to date. Ion-induced nucleation is shown to be one of the processes through which NPF initiates. Atmospheric ions act efficiently as nuclei on which organic or inorganic vapors condense, leading to the formation of new particles.

Wilson was the first to observe that water nucleates more favorably on negative ions compared to positive (negative sign-preference; Wilson 1911). Since then, many experimental studies have reported contradicting results, the origin of which is attributed mainly to the not well-defined chemical composition of the ions used in these studies.(Kangasluoma et al. 2016; Li and Hogan 2017; Winkler et al. 2008) The need exists for an experimental setup, which will reduce these uncertainties and will enable the study of such a fundamental NPF mechanism as the ion induced nucleation. Identification of the initiating mechanism of ion-induced nucleation remains, one of the most interesting open questions to date.

Furthermore, given the global scale of the NPF phenomenon, it is required to more deeply understand its origin and quantify it in terms of particle production rates. This information is crucial for global climatic models in order to be able to include more realistically the effects of particles on climate (Adams and Seinfeld, 2002; Vignati et al., 2004; Spracklen et al., 2005a,b). Although the effect of particles on climate is controlled by several physicochemical properties, the particle size holds the most significant role (Dusek et al., 2006).

Historically, aerosol instrumentation was developed for measuring particles from the μm-side of the spectrum and progressively was developed further in order to measure the size and concentration of smallest particles. The Differential Mobility Analyzer (DMA; Knutson and Whitby 1975) when coupled with a particle detector, provides a measurement of the particle size distribution, and has proven to be an invaluable tool for the study for particle size distribution related phenomena in the atmosphere (Wiedensohler et al. 2012). The most adequate detector for a DMA is the condensation particle counter (CPC), mainly due to the capability of CPC of very low concentration detection limit (i.e. 1 particle/cm^3). Although state-of-the-art DMAs are capable of measuring particle size down to the sub-1 nm range, the same is not valid for CPCs. The detection efficiency of a CPC is greatly reduced when the particle size becomes smaller than 3 nm. Nowadays, atmospheric particle research is focused on very small particles (i.e. sub-2nm size range) and this makes the need of designing and developing CPCs, that will have better performance in the sub-2nm range, even more pressing.

Recent developments in the way that atmospheric research is being conducted has created the need to develop aerosol instrumentation further. The unmanned aerial vehicle (UAV) technology has become, in the recent few years, a very popular means of performing research in the atmosphere (Altstädter et al. 2015; Neitola et al. 2017; Pajares 2015). Such technology has very low operational costs and high flexibility in terms of frequency of flights. Although UAVs are a highly matured technology, often researchers stumble upon the incompatibility of existing instruments with UAV specifications. To date, the existing DMA designs prohibit their use in airborne measurements with UAVs due to their high weight and cost.

These challenges have motivated the research that is presented in this thesis. In the following chapters, the reader may find extensive information on the challenges presented above. The work reported in this thesis aims to contribute to the field of Atmospheric Sciences by:

1) highlighting a previously unknown characteristic of the supersaturation field inside a CPC, which can be manipulated in order to significantly increase the detection efficiency for sub-2nm particles (Chapter 2).

2) introducing a new concept of manufacturing aerosol instruments and applying it to build a novel DMA of extremely low weight and production cost, with the help of 3D-printing technology (Chapter 3).

3) developing a new production method of atomic clusters under atmospheric pressure, which provides ideal seed particle for the investigation of ion-induced nucleation (Chapter 4).

4) unraveling a new behavior of sign preference in ion-induced nucleation (Chapter 5).

References

Altstädter, B., Platis, A., Wehner, B., Scholtz, A., Wildmann, N., Hermann, M., Käthner, R., Baars, H., Bange, J., Lampert, A. (2015). ALADINA–an unmanned research aircraft for observing vertical and horizontal distributions of ultrafine particles within the atmospheric boundary layer. Atmospheric Measurement Techniques 8:1627-1639.

Adams, P. J., and J. H. Seinfeld, Predicting global aerosol size distributions in general circulation models, J. Geophys. Res., 107(D19), 4370,

de España, C. D., Wonaschütz, A., Steiner, G., Rosati, B., Demattio, A., Schuh, H., Hitzenberger, R. (2017). Long-term quantitative field study of New Particle Formation (NPF) events as a source of Cloud Condensation Nuclei (CCN) in the urban background of Vienna. Atmospheric environment 164:289-298.

Dusek, U., Frank, G.P., Curtius, J., Drewnick, F., Schneider, J., Kürten, A., Rose, D., Andreae, M.O., Borrmann, S., Pöschl, U., Geophys. Res. Lett. 37 (3), (2010).

Jacobson, M. Z. (2001). Strong radiative heating due to the mixing state of black carbon in atmospheric aerosols. Nature 409:695.

Kampa, M. and Castanas, E. (2008). Human health effects of air pollution. Environmental pollution 151:362-367.

Kangasluoma, J., Samodurov, A., Attoui, M., Franchin, A., Junninen, H., Korhonen, F., Kurtén, T., Vehkamäki, H., Sipilä, M., Lehtipalo, K. (2016). Heterogeneous nucleation onto ions and neutralized ions: insights into sign-preference. The Journal of Physical Chemistry C 120:7444-7450.

Kulmala, M., Mordas, G., Petäjä, T., Grönholm, T., Aalto, P. P., Vehkamäki, H., Hienola, A. I., Herrmann, E., Sipilä, M., Riipinen, I. (2007). The condensation particle counter battery (CPCB): A new tool to investigate the activation properties of nanoparticles. Journal of aerosol science 38:289-304.

Kulmala, M., Kontkanen, J., Junninen, H., Lehtipalo, K., Manninen, H. E., Nieminen, T., Petäjä, T., Sipilä, M., Schobesberger, S., Rantala, P. (2013). Direct observations of atmospheric aerosol nucleation. Science 339:943-946.

Li, C. and Hogan, J., Christopher J (2017). Vapor specific extents of uptake by nanometer scale charged particles. Aerosol Science and Technology 51:653-664.

Neitola, K., Sciare, J., Keleshis, C., Pikridas, M., Argyrides, M., Vouterakos, P., Antoniou, P., Apostolou, A., Savvides, C., Vrekoussis, M. (2017). UAV measurements of aerosol properties at the Cyprus institute, in EGU General Assembly Conference Abstracts, 11882.

Pajares, G. (2015). Overview and Current Status of Remote Sensing Applications Based on Unmanned Aerial Vehicles (UAVs). Photogrammetric Engineering & Remote Sensing 81:281-330.

Platis, A., Altstädter, B., Wehner, B., Wildmann, N., Lampert, A., Hermann, M., Birmili, W., Bange, J. (2016). An Observational Case Study on the Influence of Atmospheric Boundary-Layer Dynamics on New Particle Formation. Boundary-Layer Meteorology 158:67-92.

Pöschl, U. (2005). Atmospheric aerosols: composition, transformation, climate and health effects. Angewandte Chemie International Edition 44:7520-7540.

Rose, C., Sellegri, K., Moreno, I., Velarde, F., Ramonet, M., Weinhold, K., Krejci, R., Andrade, M., Wiedensohler, A., Ginot, P. (2017). CCN production by new particle formation in the free troposphere. Atmospheric Chemistry and Physics 17:1529-1541.

Schobesberger, S., Junninen, H., Bianchi, F., Lönn, G., Ehn, M., Lehtipalo, K., Dommen, J., Ehrhart, S., Ortega, I. K., Franchin, A. (2013). Molecular understanding of atmospheric particle formation from sulfuric acid and large oxidized organic molecules. Proceedings of the National Academy of Sciences 110:17223-17228.

D. V. Spracklen, K. J. Pringle, K. S. Carslaw, M. P. Chipperfield, G. W. Mann. A global off-line model of size-resolved aerosol microphysics: I. Model development and prediction of aerosol properties. Atmospheric Chemistry and Physics, European Geosciences Union, 2005, 5 (8), pp.2227-2252.

Viana, M., Pey, J., Querol, X., Alastuey, A., De Leeuw, F., Lükewille, A. (2014). Natural sources of atmospheric aerosols influencing air quality across Europe. Science of the Total Environment 472:825-833.

Vignati, E., J. Wilson, and P. Stier (2004), M7: An efficient size-resolved aerosol microphysics module for large-scale aerosol transport models, J. Geophys. Res., 109, D22202,

Wiedensohler, A., Birmili, W., Nowak, A., Sonntag, A., Weinhold, K., Merkel, M., Wehner, B., Tuch, T., Pfeifer, S., Fiebig, M. (2012). Mobility particle size spectrometers: harmonization

of technical standards and data structure to facilitate high quality long-term observations of atmospheric particle number size distributions. Atmospheric Measurement Techniques 5:657-685.

Wilson, C. T. R. (1911). On a method of making visible the paths of ionising particles through a gas. Proc. R. Soc. Lond. A 85:285-288.

Winkler, P. M., Steiner, G., Vrtala, A., Vehkamäki, H., Noppel, M., Lehtinen, K. E., Reischl, G. P., Wagner, P. E., Kulmala, M. (2008). Heterogeneous nucleation experiments bridging the scale from molecular ion clusters to nanoparticles. Science 319:1374-1377.

Chapter 1

Experimental Methods

In this chapter, the main experimental methods that were used in this thesis will be presented. A general scheme, common amongst the experiments, is the usage of three main equipment categories: i) particle generation ii) particle classification and iii) particle detection. Basic operating principles will be presented, as well as bottlenecks of the state-of-the-art. Finally, the research questions will be formulated.

1.1 Particle Generation

Nanoparticles can be generated by many different methods, varying in the quality, size and composition of produced particles. What follows is an introductory analysis of the operating principles of the particle generators used in this thesis. Some generators were used as auxiliary devices, e.g. for calibration purposes, while others were the subject of extensive research and modification in order to answer the research question. Such a generator was the spark generator, which was studied extensively in chapter 4.

1.1.1 Spark Discharge Generator (SDG)

The method of producing nanoparticles by using atmospheric plasma-based electrical discharges was first introduced by Schwyn et al. (1988). Since then, the SDG has been recognized as a versatile way of producing nanoparticles and has found application in many studies.

Figure 1 shows a schematic diagram of the SDG in its most basic version. The SDG consists of a chamber which includes two electrodes of the material that is desired to produce nanoparticles out of. In order to create a potential difference, one of the electrodes remains at

ground potential while the second one is connected to a capacitor bank, charged by a high voltage power supply. When the applied voltage exceeds the breakdown voltage of the gas, a spark sequence is initiated forming a conductive channel which discharges the energy stored in the capacitors through the spark gap. The plasma created in the spark gap is unidirectional and consists of free electrons and ionized gas molecules (Vons, 2010). The heat that is dissipated on the electrode surface is suitable to evaporate atoms from the material matrix, with temperature reaching as high as 20000K (Reinmann and Akram, 1997; Tabrizi et al., 2009).
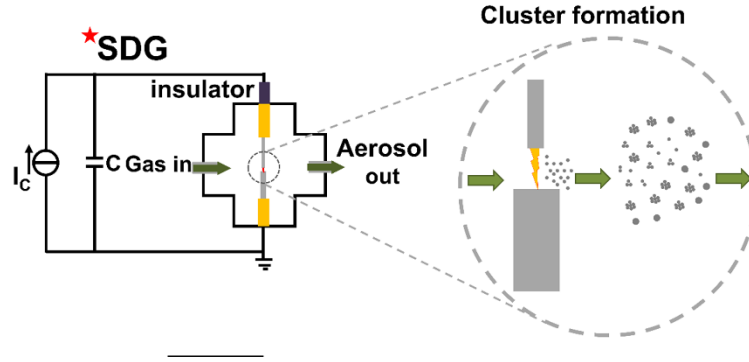
Figure 1. Schematic of the system for cluster formation by SDG showing the electrical circuit and the spark housing (cross-shaped block), I_C is the constant current to charge the capacitor C; The magnified region between the two electrodes is showing a cartoon of the particle formation process.

The cloud of evaporated atoms is then diluted by an inert gas flowing through the spark gap and is brought to room temperature. This rapid quenching of temperature is the driving mechanism for the formation of nanoparticles, through a combined process of nucleation and subsequent coagulation (Feng et al.,2016).

In every discharge, the energy E_d transferred from the capacitor bank to the spark gap is given by:

$$E_d = {CV_d^2}/{2} \quad ,$$
(1)

where V_d is the breakdown voltage of the gas. The SDG offers the possibility to adjust the mean particle size distribution by controlling only two operational parameters, the energy per spark, through the capacitance, and the flow rate. The energy per spark defines the number of atoms that evaporate from the electrodes, therefore the initial concentration available for coagulation. On the other hand, the flow rate defines the residence time of particles inside the coagulation region, and therefore the final particle size.

The simplicity of the SDG method makes it a very attractive technique for particle generation purposes. In this thesis, we used an SDG to produce the atomic clusters that were required for the investigation of the sign preference phenomenon. In chapter 4, we describe the modifications and operating conditions of the SDG that are necessary for the production of atomic clusters. With this method, we produced atomic clusters ranging from 1 to 22 atoms of silver. In Chapter 5, we describe how this improved SDG was used for experimentally measuring heterogeneous nucleation probability of polar molecules on atomic clusters and the fundamental issue of sign preference.

1.1.2 Electrospray

Electrospray is a widely studied and applied method for transferring molecules from the liquid to the gas phase. In principle, one can achieve highly monodisperse aerosol samples, by choosing the right operating conditions and liquid sample.

The simplest setup of an electrospray apparatus consists of a capillary needle housed inside a chamber, kept at ground potential. The needle is immersed inside a vial containing the liquid solution and is electrically connected to a high voltage source. Application of positive pressure drives the liquid at the capillary tip. Due to the small size of the tip (i.e. a few tens of μm), the liquid experiences a high-density electric field that "pulls" micrometer-sized droplets into the gas phase. A high number of charges is acquired by the droplets, which shortly after the tip, start to undergo evaporation and reduction of their size. When the Rayleigh radius is reached, Coulombic explosion is initiated resulting in fragmentation of the droplet. When the solvent evaporates completely, the dry residue forms a nanoparticle.

An electrospray was used for calibrating the high flow differential mobility analyzer used in most of the experimental work reported in this thesis, by using tetraheptyl ammonium bromide salt dissolved in acetonitrile (Ude and de la Mora, 2005). In addition, an electrospray was also used as a particle generator of sub-2nm particles of Tetrabutylammonium and the bromide ion.

1.1.3 Glowing wire

Similarly to the spark generator, the operating principle of the glowing wire generator relies on an evaporation/condensation process. In this generator, evaporation comes from resistively heating a piece of metal wire, by passing high current through it (Peineke and Schmidt-Ott,2008; Peineke et al., 2006; Schmidt-Ott et al., 1980). The evaporated cloud of atoms is quenched by a flow of gas which carries the particles out of the housing chamber.

In this thesis, a home-made glowing wire generator was used in chapter 4 and provided the test particles with which the transfer function of the lightweight DMA was evaluated in a TDMA experimental setup.

1.2 Differential Mobility Analyzer

The differential mobility analyzer (DMA) is a core instrument in aerosol research, which when combined with a particle detector, provides a measurement of the size distribution of particles. A DMA can be used also for producing a monodisperse particle flow that can be used for various purposes like understanding the particle dynamics, particle deposition on substrates or calibration purposes.

The operating principle on which size classification is achieved, is surprisingly simple. Although DMAs of various designs exist, we are using a cylindrical DMA to explain the operating principle. Figure 2 shows a schematic diagram of a cylindrical DMA. The polydisperse aerosol enters the DMA though a slot at the outer cylinder with a flow rate Q_a and the charged particles are either reflected or attracted from the central rod, due to the existence of an electric field. A stream of sheath air flows along with the aerosol flow with a flow rate Q_s. The particles that are being attracted follow parabolic trajectories towards the central rod and eventually they will collide with it. The distance that they will cover along the axis of the inner rod, is a function of their electrical mobility, of the voltage applied to the rod and of the flow rates Q_s and Q_a (Knutson and Whitby, 1975).
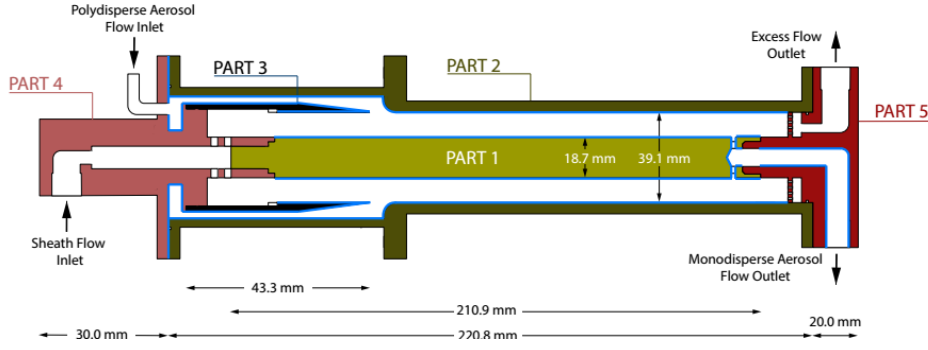
Figure 2. Schematic diagram of cylindrical type DMA.

By controlling the voltage and the flow rates, particles with a narrow distribution of electrical mobilities exit the slit located at the end of the central rod, where a detector is placed for counting the concentration. Knutson & Whitby (1975) showed that this distribution has an upper and a lower limit. The upper limit corresponds to particles that enter to the outermost radial position on the aerosol inlet and reach the monodisperse slit at its beginning. Such particles will have an electrical mobility equal to:

$$Z_{max} = \frac{Q_a + Q_s}{2\pi r_1 E_1 L} \qquad (1)$$

The lower limit corresponds to particles that enter the classification region at the innermost position of the aerosol inlet and just reach the central rod at the end of the slit opening. Such particles will have an electrical mobility equal to:

$$Z_{max} = \frac{Q_a - Q_s}{2\pi r_1 E_1 L}, \qquad (2)$$

where r_1 is the radial position of the surface of the inner rod, measured from the axis of the rod. Between these two limits, particles with intermediate mobilities will reach the slit and contribute to the measured size distribution. The weight of this contribution is estimated through the DMAs' transfer function, Ω. The transfer function is defined as the probability that an entering particle, with electrical mobility Z, will have the correct trajectory to exit through the exit slit with the classified aerosol (Knutson & Whitby, 1975).

An ideal DMA with an ideal transfer function would produce only one size of aerosol when set at a constant voltage. In reality, there is a narrow distribution of sizes which exit the DMA at a set voltage. The width of this distribution can be controlled by the ratio of sheath-air to sample aerosol. The higher the ratio of sheath to sample air, the narrower the resulting size distribution will be.

Losses in the inlet and outlet regions outside the classification zone are not included in Ω. In this case the plot of the transfer function against the electrical mobility is a triangular shaped function. If diffusion broadening of the particle trajectories is to be considered, the transfer function broadens, thus including particles within a wider range of mobilities that can exit the DMA slit and contribute to the aerosol distribution (Stolzenburg & McMurry, 2008).

The first experimental work using electrical mobility analysis dates back to the first half of the 20th century. Based on an earlier design by Zeleny (1900), a DMA was developed by Erikson (1921) and used for studying the aging of ions in gases and in the atmosphere. Later, Rohmann (1923) used this method to measure the size distribution of airborne particles. Major improvements that followed by Hewitt (1957) have led to the DMA that we know today. The cylindrical DMA is the most recognizable design of all that exist, mainly due to the work of Whitby and Clark (1966) who set the ground for the commercial version of the instrument known as the Electrical Aerosol Analyzer (EAA; Liu and Pui 1974;1975). A comprehensive theoretical understanding of the operation of the DMA was given later by Knutson and Whitby (1975), who introduced the concept of the DMA transfer function and resolution. All of these DMAs though suffered from very low resolution when measuring particles smaller than 10 nm. In the years that followed, significant effort was put to develop DMAs that would perform better in that size range. It was identified that in order to achieve this goal it was necessary to redesign the DMA to facilitate operation at much higher flow rates. Nowadays DMAs that have significantly high resolution in the sub-2nm range exist (Rosell-Llompart et al., 1996; Seto et al., 1997; de Juan and de la Mora, 1998; Rosser and de la Mora, 2005)

The history of the DMA development is full of extremely interesting studies and modifications that have increased the measuring capabilities of the instrument, and therefore its value for research. This has been recognized by the scientific community and DMAs are being used for a variety of different research studies. The most relevant application to this thesis is the atmospheric and air pollution research. DMAs are being used as monitoring equipment for urban air pollution, monitoring pristine environments, filtration studies, automotive exhaust studies and many more. There are a few aspects of the DMA than remain to be improved though. DMAs are constructed out of metal, therefore they tend to be heavy and require an expensive manufacturing process. This fact hinders the widespread application of this instrument. For example, it is acknowledged that in order to measure more accurately the urban air pollution, it is necessary to establish a dense network of monitoring stations, which currently is not possible due to the associated high cost. Low cost sensors are needed in order to facilitate such a goal. In addition, a

whole new way of conducting atmospheric airborne measurements is emerging with the use of UAVs. The current instruments do not fulfill the weight specifications that the UAV inherently poses, they are too heavy and bulky. Light-weightness and portability are characteristics that are highly needed in the next generation of DMAs.

The work described in Chapter 3 of this thesis is devoted in covering this need by introducing a new method of manufacturing DMAs. The key concept behind the new method is that the electrical conductivity that is required for the operation, is not needed throughout the whole body of the DMA. Therefore, it is possible to construct the DMA out of any low-cost and low-weight material and apply a conductive layer only on the inside surfaces, through which the aerosol flow is exposed. Following this concept, we built a DMA out of polyurethane and compared its performance with an identical DMA made out of stainless steel. The new DMA is extremely lightweight (<100gr) making it ideal for incorporation inside a UAV. Overall, this new method offers the possibility of producing lightweight DMAs, but also offers a new way with which prototypes can be tested. By removing the necessity of a fully equipped workshop to process metal, and instead using a 3D printer for production, prototypes can be easily manufactured at a very low cost. Of course, this method is not limited to DMAs. In any aerosol instrument, it is necessary to have conductive surfaces in order to avoid charge accumulation and therefore increase of particle losses. Therefore, this method can be applied to a variety of aerosol instruments, boosting the research and innovation in aerosol instrumentation significantly.

1.3 Condensation Particle Counter

Optical detection of particles is a reliable and robust method for counting particles and relies on a simple operating principle. When particles transverse through a beam of light they scatter and absorb the radiation. The intensity of scattered radiation can be detected by a photodetector as a sequence of light pulses. The number of pulses corresponds to the number of particles present in the sample. The main limitation of this method is that it cannot be applied for particle sizes smaller than circa 200 nm. The scattering intensity decreases rapidly as particle size becomes smaller, making the signal indistinguishable from the signal noise.

Condensation Particle Counters (CPCs) were developed to overcome this limitation. They do so, by applying a very simple and ingenious solution. Particles are artificially grown to micrometer sized droplets before they reach the optical detector. The artificial growth is achieved by vapor condensation on the particle surface. Whether a particle will be activated (i.e. initiate

vapor-to-liquid phase transition) is dependent on various parameters of the liquid properties (vapor pressure, surface tension) and of the particle (e.g. particle size, chemical composition, charge). The theory describing the activation probability has been used extensively in CPC studies (described in detail in Chapter 2), and good agreement with experimental results has been achieved.

The main limitation of existing CPCs is that particle sizes below as certain critical size will get activated with a probability smaller than 1. The probability of activation decreases with decreasing particle size. Therefore, it follows that the detection efficiency of the CPC will be smaller than 100%, resulting in underperformance of the instrument.

Fueled by this limitation, a lot of research has been conducted in the past resulting in pivotal moments in the history of the development of CPCs. Three main categories of CPCs exist, namely the expansion, mixing and laminar flow CPC. What differentiates these types is the method used to initiate phase transition. In expansion type CPCs, supersaturation is achieved by rapid expansion of a volume of sample which is saturated with vapors of the working fluid. Rapid expansion creates a temperature drop throughout the whole volume of the sample, resulting in a uniform supersaturation field. This constitutes the main advantage of expansion type CPCs because all particles are exposed to the same supersaturation value. Mixing type CPCs, as the name implies, achieve supersaturation by mixing the sample flow saturated with vapors, with another lower temperature flow. Kousaka et al. (1982) built the first mixing CPC capable of sub-10 nm particle detection.

The majority of CPCs used by aerosol research groups is a laminar flow type (Bricard et al.,1976), and thus due to relevance, improving their performance is of high importance. This type of CPC uses diffusion and convection cooling in order to create supersaturation. Figure 3 shows the schematic diagram of the internal tubing of a CPC (model 3025, TSI). Sample enters the aerosol inlet and is split into two flows. One of them passes through an orifice and meets the second flow, which is saturated in vapors (e.g. butanol) and has been filtered to remove all particles. In addition, the secondary flow serves the purpose of sheathing the aerosol flow and containing particles in the centerline of the tube. Inside the condenser tube, which is maintained at a lower temperature than the saturated flow, phase transition is initiated, and vapors condense on the particle surface.
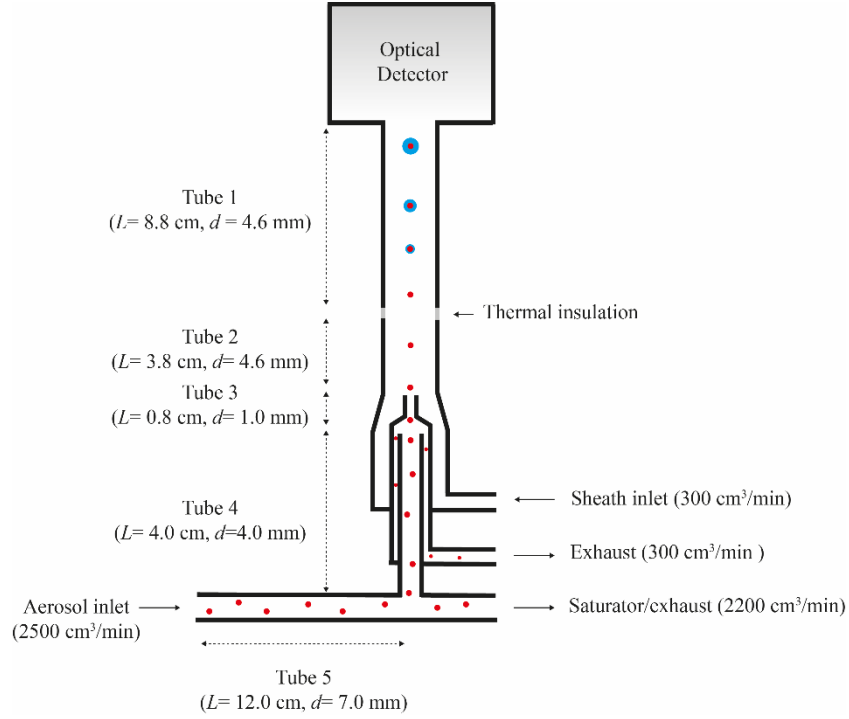
Optical
Detector

Tube 1
(L= 8.8 cm, d = 4.6 mm)

← Thermal insulation

Tube 2
(L= 3.8 cm, d= 4.6 mm)

Tube 3
(L= 0.8 cm, d= 1.0 mm)

Tube 4
(L= 4.0 cm, d=4.0 mm)

← Sheath inlet (300 cm³/min)

→ Exhaust (300 cm³/min)

Aerosol inlet →
(2500 cm³/min)

→ Saturator/exhaust (2200 cm³/min)

Tube 5
(L= 12.0 cm, d= 7.0 mm)

Figure 3. Schematic layout of the TSI 3025 CPC, showing the length L and diameter d of the tubing through which the sampled aerosol flows.

The laminar flow CPC is the most used CPC since it has been commercially available for many decades. Later, Stolzenburg and McMurry (1991) optimized the design of the laminar flow CPC by introducing a sheath air flow and achieved sub-3nm particle detection. Their modifications focused on reducing particles losses by bringing particles close to the centerline of the condenser tube where the maximum supersaturation is achieved. This innovation was commercialized by TSI by producing the ultrafine-CPC which has become one of the most popular CPC instruments. The next major milestone in improving the detection efficiency of ultrafine CPCs was the work of Mertes et al. (1995), in which they reported significant increase of the detection efficiency by simply increasing the difference between the operating temperatures of the condenser and saturator of the CPC. This meant that the CPC could very easily be "boosted" to detect a new range of particle sizes, without any hardware modifications.

In this work, we developed a new method for increasing the detection efficiency of laminar flow CPCs. We did that by focusing on an aspect of the operation that had been overlooked or neglected by previous studies. This aspect is the volume which the supersaturation profile occupies inside the condenser tube. We found that by choosing the right absolute operational temperatures of the CPC, the spatial characteristics of the supersaturation profile can be controlled with high

resolution. This discovery has led to a new way of operating CPCs, which we refer to as Temperature Window operation. The results of the Temperature Window method are described in detail in Chapter 2. The benefit of this method is two-fold. On one hand, it can increase the detection efficiency of a CPC by 40% and on the other hand it shines light on an aspect of the CPC operation that was not considered in the past, which will aid to the design of CPCs optimized for the detection of sub-2nm particles.

References

Bricard, J., Delattre, P., Madelaine, G., and Pourprix, M.. Detection of ultra-fine particles by means of a continuous flux condensation nuclei counter, Fine Particles, Academic Press, New York, 565-580, 1976.

de Juan, L. and Fernandez de la Mora, J. 1998. High resolution size-analysis of nanoparticles and ions: Running a DMA of near optimal length at Reynolds numbers up to 5000. Journal of Aerosol Science. 29(7), 617-626.

Erikson, H. A.: The Change of Mobility of the Positive Ions in Air with Age, Phys. Rev., 18, 100-101, 1921.

Feng, J., Huang, L., Ludvigsson, L., Messing, M.E., Maisser, A., Biskos, G., and Schmidt-Ott, A.(2016). General approach to the evolution of singlet nanoparticles from a rapidly quenched point source. J. Phys. Chem. C, 120(1):621–630.

Hewitt, G. W.: The charging of small particles for electrostatic precipitation, American Institute of Electrical Engineers Transactions, 76, 300-306, 1957.

Knutson, E., and Whitby, K.: Aerosol classification by electric mobility: apparatus, theory, and applications, J Aerosol Sci, 6, 443-451, 1975.

Kousaka, Y., Niida, T., Okuyama, K., and Tanaka, H.: Development of a Mixing TypeCondensation Nucleus Counter, J Aerosol Sci, 13, 231-2401982.

Liu, B.Y.H. and Pui, D.Y.H. 1974. A submicron aerosol standard and the primary, absolute calibration of the condensation nuclei counter. Journal of Colloid and Interface Science. 47, 155-171.

Liu , B.Y.H. and Pui , D.Y.H. 1975. On the performance of the electrical aerosol analyzer. Journal of Aerosol Science. 6, 249-264.

Mertes, S., Schroder, F., and Wiedensohler, A.: The Particle-Detection Efficiency Curveof the Tsi-3010 Cpc as a Function of the Temperature Difference between Saturator andCondenser, Aerosol Sci Tech, 23, 257-261, Doi 10.1080/02786829508965310, 1995.

Peineke C., Attoui M., Schmidt-Ott A. (2006). Using a glowing wire generator for the production of charged, uniformly sized nanoparticles at high concentrations J.Aerosol Sci., 37, 1651-1661

Peineke, C., Schmidt-Ott, A. (2008). Explanation of Charged Nanoparticle Production from Hot Surfaces. J. Aerosol Sci., 39:244–252.

Reinmann, R., Akram, M. (1997). Temporal Investigation of a Fast Spark Discharge in Chemically Inert Gases. J. Phys. D—Appl. Phys., 30:1125–1134.

Rohmann, H. 1923. Methode zur Messung der Grösse von Schwebeteilchen. Zeitschrift fur Physik. 17, 253-265.

Rosell-Llompart, J., Loscertales, J.G., Bingham, D. and Fernandez de la Mora, J. 1996. Sizing nanoparticles and ions with a short differential mobility analyzer. Journal of Aerosol Science. 27(5), 695-719.

Rosser, S. and Fernandez de la Mora, J. 2005. Vienna-type DMA of high resolution and high flow rate. Aerosol Science and Technology. 39, 1191-1200.

Schmidt-Ott, A., Schurtenberger, P., Siegmann, H. C. (1980). Enormous Yield Of Photoelectrons From Small Particles. Phys. Rev. Lett., 45:1284–1287.

Schwyn, S., Garwin, E., and Schmidt-Ott, A. (1988). Aerosol Generation by Spark Discharge. J. Aerosol Sci., 19:639–642.

Seto, T., Nakamoto, T., Okuyama, K., Adachi, M., Kuga, Y. and Takeuchi, K. 1997. Size distribution measurement of nanometer-sized aerosol particles using DMA under low-pressure conditions. Journal of Aerosol Science. 28(2), 193-206.

Stolzenburg, M. R., and McMurry, P. H.: Equations governing single and tandem DMA configurations and a new lognormal approximation to the transfer function, Aerosol Sci Tech, 42, 421-432

Stolzenburg, M. R., and McMurry, P. H.: An Ultrafine Aerosol Condensation Nucleus Counter, Aerosol Sci Tech, 14, 48-65, 1991.

Tabrizi, N. S., Ullmann, M., Vons, V. A., Lafont, U., Schmidt-Ott A. (2009). Generation of Nanoparticles by Spark Discharge. J. Nanoparticle Res., 11:315–332.

Ude, S., and de la Mora, J. F.: Molecular monodisperse mobility and mass standards from electrosprays of tetra-alkyl ammonium halides, J Aerosol Sci, 36, 1224-1237.

Vons, V. A. (2010). Spark Discharge Generated Nanoparticles for Hydrogen Storage Applications. PhD thesis, Delft University of Technology, Delft, The Netherlands.

Whitby, K. T. and Clake, W. E. 1966. Electric aerosol particlecounting and size distribution measuring system for the 0.015 to 1 μm size range. Tellus. 18, 573-586.

Zeleny, J.: The Velocity of the Ions Produced in Gases by Röntgen Rays, Phil. Trans. Roy. Soc.
    A., 195, 193-234, 1900.

Chapter 2

Enhancing the detection efficiency of condensation particle counters for sub-2nm particles

Abstract

The detection efficiency of Condensation Particle Counters (CPCs) reduces drastically as particle size becomes smaller than 2 nm. Increasing the supersaturation in order to enhance the detection efficiency, has limited applicability because the onset supersaturation value of droplet formation by homogeneous nucleation is very close to the heterogeneous onset supersaturation for sub-2 nm particles. In this work we introduce a new method for increasing the detection efficiency of CPCs for sub-2 nm particles, which relies mainly on controlling the spatial distribution of the supersaturation profile by simply modifying the operating temperatures of the CPC. We evaluated the new method by generating monodisperse particles in the size range of 0.98 to 4.50 nm and used them to characterize a TSI 3025 CPC. We achieved significant increase of the detection efficiency for sub-2 nm particles. Furthermore, we calculated the supersaturation field developed in the condenser tube with a finite element model and used it to determine the detection efficiency according to heterogeneous nucleation theory. These calculations reveal that the observed increase of the detection efficiency can be explained by the manipulation of the spatial distribution of the supersaturation field. The method introduced here can greatly improve the detection efficiency of CPCs and in the meantime further extend their use for particle sizing purposes in the sub-2-nm range.

2.1 Introduction

Observations of nucleation events in the atmosphere are important for better understanding the physical processes governing the evolution of the size distribution of aerosol particles, and thus for improving the predictability of climate models. In these observations, measurements of the concentration of particles smaller than 2 nm are of particular importance for understanding the early stages of particle formation and their subsequent growth. Due to their highly diffusive nature, however, the detection of particles having sizes in that range can be challenging, especially in the context of atmospheric observations where their concentrations can be relatively low (Kulmala et al., 2013).

Condensation Particle Counters (Agarwal & Sem, 1980; Bricard et al., 1976; McMurry, 2000; Stolzenburg & McMurry, 1991) have been widely used for measuring the concentration of airborne nanoparticles. Compared to an aerosol electrometer (Liu et al., 1974), CPCs have an extremely high counting sensitivity because, in principle, they have the capability of single-particle detection. In addition, CPCs are unique detectors of uncharged particles, a fact that is especially valuable for studies of the atmospheric aerosol (Kulmala et al., 2004).

One limitation of CPCs is that their detection efficiency decreases substantially when particle size decreases below a threshold value. Smaller particles require a higher supersaturation in order to initiate condensational growth, because the equilibrium vapor pressure over a curved surface is higher than that over a flat surface (Kelvin effect). The 50% detection efficiency of standard CPCs is ca. 10 nm (e.g., for the TSI Model 3010). A recent study has shown that by modifying the operating conditions of the TSI Model 3772, detection of sub-2 nm particles is possible with surprisingly high detection efficiency (Kangasluoma et al., 2015a). In the case of ultrafine CPCs, the 50% detection efficiency is achieved for particles having sizes close to 2.5 nm (e.g. TSI Models 3025 and 3776; (Kuang et al., 2012; Stolzenburg & McMurry, 1991). Parallel to these developments, state-of-the-art aerosol classifiers can already size sub-2 nm particles and atomic clusters with extremely high resolution (De Juan & Fernández de la Mora, 1998; Maisser et al., 2015; Rosser & Fernández de la Mora, 2005; Rus et al., 2010). As a result, CPCs with higher detection efficiencies than those of commercial systems are needed for integrating them in spectrometers capable of measuring the size distributions of particles in the sub-2 nm range.

A number of studies have looked into further increasing the detection efficiency of CPCs leading to the development of several instruments able to detect particles in the sub-2 nm range (Iida et al., 2009; Kulmala et al., 2007; Lehtipalo et al., 2009; Mordas et al., 2005; Saghafifar et al.,

2009; Seto et al., 1997; Sgro & Fernández de la Mora, 2004; M Sipilä et al., 2009; Mikko Sipilä et al., 2008; Vanhanen et al., 2011). A common feature in many studies is that the detection efficiency of a CPC is enhanced by augmenting the temperature difference between the saturator and the condenser tube (Hermann & Wiedensohler, 2001; Kuang et al., 2012). Increasing the temperature difference increases the supersaturation in the condenser tube, which in turn increases the activation probability of the smaller particles. Other studies have focused on the use of working fluids other than butanol, aiming to take advantage of their different physical behavior during nucleation (Magnusson et al., 2003). Iida et al. (2009) pointed out that an ideal working fluid for activation of small ions should have a high surface tension and low vapor pressure.

In thermally diffusive laminar flow CPCs, the supersaturation profile developed inside the condenser has a non-uniform spatial distribution with values ranging from 1 (i.e. saturation) up to some maximum value determined by the operating conditions of the instrument. Given that particles follow a convective-diffusive trajectory inside the condenser, a certain fraction of their population will not traverse regions at which the supersaturation is high enough for activation. Controlling the spatial distribution of the supersaturation profile could increase the fraction of particles traversing regions where they can activate, thereby providing a new way of increasing the particle activation probability and therefore the detection efficiency of CPCs.

In this article, we introduce a new controlling parameter for increasing the detection efficiency of continuous laminar flow CPCs, which relies on manipulating the spatial distribution of the supersaturation profile by taking advantage of the nonlinear dependence of the supersaturation on temperature. We call this new parameter temperature window (TW), defined by the location of the temperature difference between the saturator and condenser (ΔT) in the temperature domain. We have identified that for a given constant ΔT, variation of the spatial distribution of the supersaturation profile can be achieved by choosing different TWs. This variation was found to have significant impact on the detection efficiency of sub-2 nm particles. We tested different TWs on a butanol-based ultrafine CPC (TSI Model 3025) and report the measured detection efficiency for various particle sizes in the 0.94-4.5 nm mobility diameter range. In addition, we provide a theoretical explanation of the observed effect, using a simple model of the CPC detection efficiency.

2.2 Simulations

2.2.1 Background

The operating principle of CPCs relies on the exposure of the sampled particles to a supersaturated vapor (e.g. butanol), thereby initiating condensation of vapors on the surface of the particles. Three methods are used for creating the required supersaturation: 1. expansion of a saturated flow (Wagner, 1985), 2. mixing of cold and warm saturated flows (Kousaka et al., 1982), and 3. thermally diffusive laminar flow cooling (Bricard et al., 1976; Stolzenburg & McMurry, 1991). The latter is applied in the majority of commercial CPCs, and thus the following discussion is restricted to this method. In order to create the required supersaturation, the sampled aerosol gets saturated in vapors by passing it through the saturator tube that contains the working fluid maintained at a constant temperature. The saturated flow then enters the condenser tube, which is maintained at a lower temperature than that of the saturator, in order to create the required temperature difference for supersaturation to occur. The condensing vapors increase the particle diameter to the micron size range, which can then be easily detected by optical methods (light scattering).

The detection efficiency η of a CPC is defined as the ratio of number concentration of the detected particles N_{CPC} over the total particle number concentration at the inlet of the CPC N_{total}:

$$\eta = N_{CPC}/N_{total} \ ,$$
(1)

and depends primarily on the activation probability of particles, which is mainly a function of the supersaturation and the particle diameter. In addition, the chemical composition and the charge state of the particles (i.e. number of charges and polarity) has an important effect on their activation probability.

Diffusional particle losses inside the tubing of the CPC comprise another important process defining η, especially for particle sizes smaller than 2 nm. N_{total} is usually measured at the inlet of the CPC. As a result, the number of particles that reach the inlet of the condenser tube is smaller than the N_{total} value measured at the inlet of the CPC. Both activation probability and diffusional particle losses inside the CPC are captured by our model and are discussed in the following subsections.

2.2.2 Particle activation probability

Particle growth by condensation occurs inside the condenser tube, in which a profile of supersaturated butanol vapor is developed as a result of the cooling of the incoming saturated flow. The saturation ratio S is defined as the ratio of partial vapor pressure P_{vap} over the equilibrium partial pressure $P_{sat,T}$ at any given gas temperature T:

$$S = P_{vap}/P_{sat,T} \ . \tag{2}$$

Particles passing through the condenser provide the necessary surface energy for heterogeneous nucleation. Vapor molecules then pass from the gas to the liquid phase via condensation on the surface of the particles, leading to the formation of larger droplets. Classical nucleation theory can be used to determine the droplet formation rate, resulting from heterogeneous nucleation, as follows (Fletcher, 1958):

$$J_{het} = J_{het}^0 \exp(-\Delta G_{het}^*/k_b T) \ . \tag{3}$$

Here ΔG_{het}^* is the formation free energy of the critical droplet size, k_b is the Boltzmann constant, T is the gas temperature and $J_{het}^0 = \pi d_p^2 10^{29}$ is a kinetic pre-exponential factor (cf. Fletcher, 1958), where dp is the dry particle diameter.

The formation free energy is accordingly calculated taking into consideration that the particles are charged. The charge-dipole interactions between the charged particles and the vapor molecules becomes significant for particle sizes smaller than 2 nm. The electrostatic attraction reduces the supersaturation required to promote nucleation as compared to heterogeneous nucleation in the case of a neutral particle. The change in Gibbs free energy during the formation of a droplet on an charged particle or cluster of atoms is given by (Thomson, 1888):

$$\Delta G = 4\pi r^2 - (4\pi/3V) \, r^3 kT \ln S - (ne)^2 (1 - 1/\varepsilon)(1/8\pi\varepsilon_0)(1/r_0 - 1/r) \,, \tag{4}$$

where r is the critical droplet radius, V is the molecular volume of the liquid, ε_0 is the dielectric constant of the condensing liquid, r_0 is the radius of the seed particle, n is the number of elementary charges carried by the particles, and e is the elementary electron charge. The first and second term express the Kelvin effect while the third term express the electrostatic interaction between the charged particle and vapor molecule. Heterogeneous nucleation probability P can then be calculated by:

$$P = 1 - exp(-J_{het}t),\tag{5}$$

where t is the residence time of the particle in the nucleation zone. Particles were considered activated when their nucleation probability exceeded 50%. Particles were considered fully wettable (i.e. vapor-particle contact angle equal to zero) and surface tension dependence on temperature was taken into account (Dean, 1999).

2.2.3 Supersaturation profile

A two dimensional axisymmetric model was developed in COMSOL Multiphysics simulation software, that solves the coupled heat and mass transfer equations for incompressible flow (Naiver-Stokes) for determining flow, temperature and concentration profiles of the working fluid (i.e. butanol) within the condenser (Stolzenburg & McMurry, 1991). Vapor concentration at the wall of the condenser was set equal to the saturated concentration corresponding to the wall temperature value (i.e. perfectly wetted wall). The tube walls were treated as temperature boundaries, with thermal insulation at the contact points between the saturator and condenser tube. The sheath Q_s and aerosol flow rate Q_a were fixed at 300 cm³/min and 33 cm³/min, respectively, resulting in a total flow rate of 333 cm³/min in the condenser tube. All tubes had cylindrical geometry and fully developed laminar flow was assumed throughout the calculation domain. In principle, growth of activated particles can lead to a decrease of vapor concentration (vapor depletion by condensation on the seed particles) if their concentration is high, which in turn can reduce the supersaturation inside the condenser and thus decrease the detection efficiency. This process was experimentally evaluated, and the effect of vapor depletion was found to be negligible and therefore not included in the model calculations (cf. Supplementary information). Although, latent heat release during condensation of vapors can reduce locally the value of supersaturation, this effect was not included in the calculations.

Under the assumption that butanol vapor behaves as an ideal gas, the partial pressure of butanol vapors can be determined by the concentration and the temperature profile calculated numerically. Figure 1 shows a typical supersaturation profile in the condenser; only the condenser tube domain is shown here because the flow at its inlet was calculated to be saturated in butanol vapors under the specific operating conditions. Maximum supersaturation is achieved close to the centerline of the condenser tube. As a result, particles that deviate from the centerline will not be exposed to the maximum supersaturation, thereby reducing their activation and detection probability.
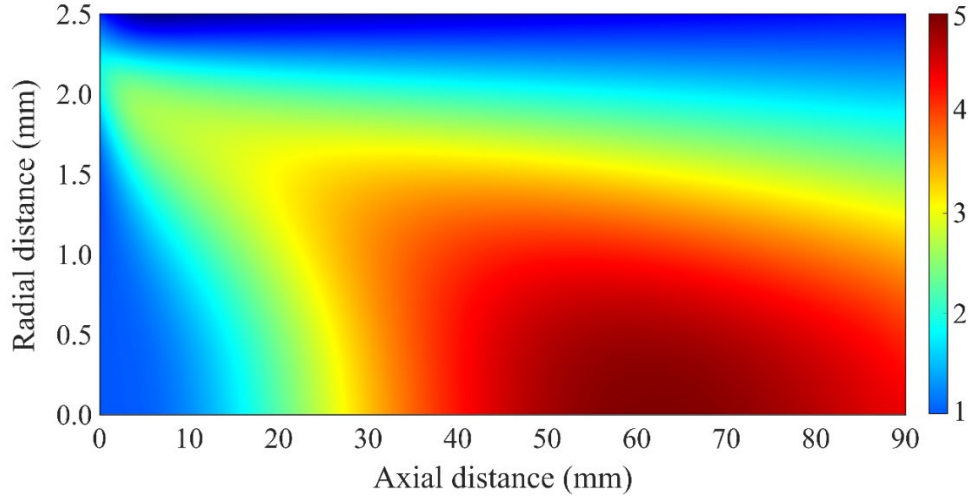
Figure 1. Supersaturation profile developed inside the condenser tube of a 3025 TSI CPC, operated at $\Delta T = 32$ °C, $T_c = 10$ °C and $T_s = 42$ °C.

2.2.4 Particle transport losses

In order to calculate the diffusional losses of the particles within the TSI 3025 CPC, we measured the length and diameter of the five tubes through which the sampled aerosol passes. A simplified schematic layout of the entire aerosol path, along with its dimensions, is shown in Figure 2. The diffusional losses for particles of different sizes passing through each tube were calculated using the well-established equation proposed by Gormley and Kennedy (1948) and appropriate values of tube geometry and flow rate.

When particles are activated inside the condenser tube (Tube 1 in Figure 2), they grow into micron-sized droplets, for which the diffusional losses can be safely neglected. Diffusional losses in Tube 1 were calculated up to the axial point were supersaturation becomes critical for particles of a given size to activate.
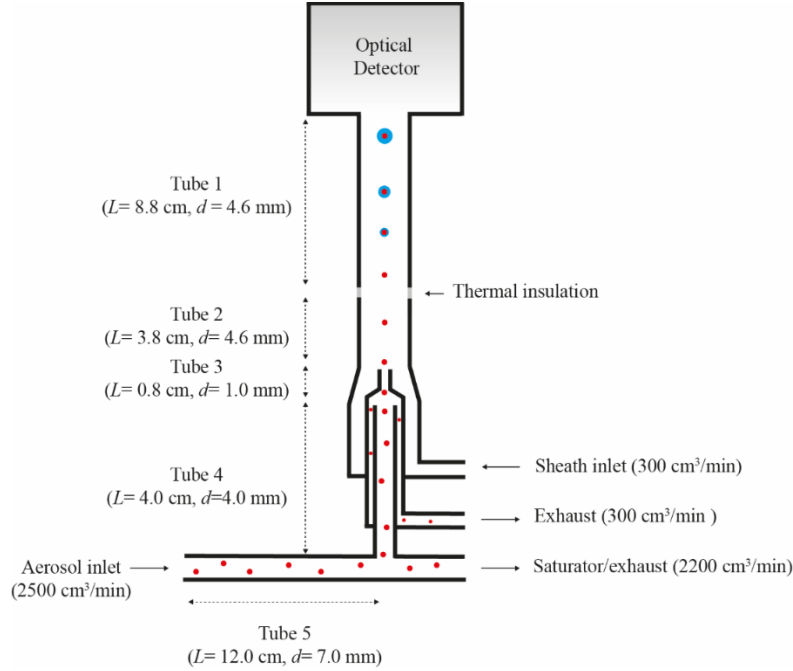
Figure 2. Schematic layout of the TSI 3025 CPC, showing the length L and diameter d of the tubing through which the sampled aerosol flows.

2.3 Experimental

Figure 3 shows the experimental setup used to measure the detection efficiency of the TSI 3025 CPC operated under a varying temperature window scheme. A custom-made electrospray source (ES; Ude & Fernández De la Mora, 2005) designed by one of us (Attoui@u-pec.fr) was used to produce tetraheptylammonium bromide (THABr; Sigma Aldrich) and tetrabutylammonium bromide (TBABr; Sigma Aldrich) ionic mobility standards for the tests. The electrospray was operated with a constant nitrogen flow through the ES chamber, and the applied pressure over the liquid solution was kept constant by using a syringe pump. This generation method produced a steady concentration of monomobile, positively or negatively charged particles covering a mobility diameter range from 0.94 to 1.73 nm.

Nickel particles larger than 2 nm were generated using a custom-made glowing wire generator (GW; (Peineke et al., 2006). In the GW generator, high current was passed through a Ni wire, causing significant resistive heating and material evaporation from its surface. The resulting metallic vapor cloud was then cooled and diluted by a constant nitrogen flow, forming aerosol particles by nucleation and subsequent condensation.

The singly self-charged generated particles were then classified based on their electrical mobility by passing them through a high flow differential mobility analyzer (half-mini DMA; (De Juan & Fernández de la Mora, 1998; Fernández de la Mora et al., 1998; Fernández de la Mora & Kozlowski, 2013; Kangasluoma et al., 2014; Maißer et al., 2015; Maißer et al., 2011; Wang et al., 2014). Mobility classification was achieved by operating the half-mini DMA at a high sheath flow rate in a closed sheath loop configuration. The half-mini DMA was calibrated using the positive monomer of the THAB particles produced by the ES. These particles have an electrical mobility Z of 0.971 Vs/cm^2 in N$_2$ (Ude & Fernández De la Mora, 2005).

Following classification, the concentration of the monodisperse aerosol particles at the outlet of the DMA was measured in parallel by the CPC and by an aerosol electrometer (AEM), in order to determine respectively N_{cpc} and N_{total} used in Equation 1. The AEM consisted of a custom-made aluminum Faraday cage and a hot electrode that was connected to a sensitive electrometer (Keithley Model 6517B). In order to ensure that the particle transport losses in the tubes leading to the detectors was the same, the two parallel paths were of identical length and the sampling flow rates of both were set to 2.5 lpm. For each particle size the AEM and CPC concentration signals were recorded for a minimum of 2 min in order to monitor the stability of the concentration produced by the ES.
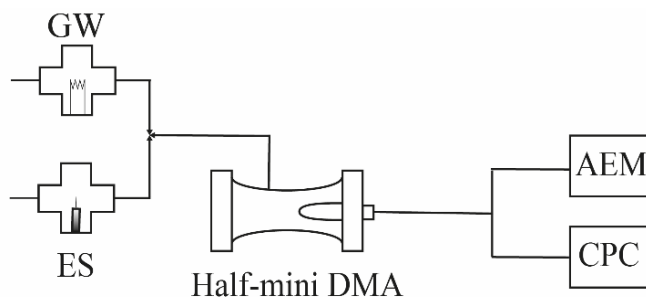
Figure 3. Schematic layout of the experimental setup used for measuring the detection efficiency of the CPC. Key: AEM, Aerosol Electrometer; CPC, Condensation Particle Counter; ES, Electrospray Source.

Detection of sub-2 nm particles is not feasible under the default operating conditions of the CPC. Two major modifications were applied to the instrument in order to increase η. Firstly, ΔT was increased from 27 °C (i.e. default operating conditions) to 32 °C in order to increase the supersaturation in the condenser tube and thus the particle activation probability. Secondly, the sheath and aerosol flows were set to 300 cm^3/min and 33 cm^3/min, respectively. Homogeneous

nucleation rate at these conditions was below 1 particle per minute, at all temperature settings. In addition, the inlet sampling flow rate of the CPC was increased from its default value of 1.5 lpm to 2.5 lpm. This was done in order to reduce particle diffusional losses in the tubing from the DMA to the inlet of the CPC, and to match the flow rate of the AEM thereby ensuring equal transport losses for the two detectors. The detection efficiency of the CPC for each particle size was determined at 5 different TWs, indicated by the absolute condenser and saturator temperature in the nomenclature (e.g. TW-2-34 is the temperature window with $T_c = 2$ °C and $T_s = 34$ °C). The temperature of the optics was kept always 1°C higher than the saturator temperature, in order to avoid vapor condensation inside the optics chamber. Table 1 summarizes the modified operating conditions as well as the experimental measurement scheme in each experiment.

Table 1. Summary of the modified operating parameters used for enhancing the detection efficiency of the CPC under different temperature windows. Also shown are the default operating parameters. Key: T_c, condenser temperature; T_s, saturator temperature; ΔT, temperature difference between condenser/saturator; Q_a, aerosol flow rate; Q_s, sheath flow rate.

Temperature Window	T_c (°C)	T_s (°C)	ΔT (°C)	Q_a (cm³/min)	Q_s (cm³/min)
TW-2-34	2	34			
TW-4-36	4	36			
TW-6-38	6	38			
TW-8-40	8	40	32	33	300
TW-10-42	10	42			
Default	10	37	27	30	270

In order to ensure that vapor depletion in the saturator is negligible and thus it does not affect the detection efficiencies measured at the different TWs, we performed preliminary measurements using positive THA⁺ monomers (1.47 nm) at various initial concentrations. By varying the liquid-solution flow rate through the ES source we produced sample aerosols having particle number concentrations of 10^3, 10^4, and 10^5 #/cm³, and used them to measure the detection efficiency of the CPC operated at 5 temperature window settings. At the highest concentration (i.e., 10^5 #/cm³), the

decrease of η ranged from 14.5 to 34.6% when the TW was varied from TW-2-34 to TW-10-42. When the concentration was fixed to 10^3 and 10^4 #/cm³, however, η remained constant (within experimental uncertainty) for the different TWs (cf. Figure S1; Supplemental information). Following these tests, all the subsequent measurements of η reported in the rest of the paper were carried out with an initial particle concentration of 10^3 #/cc.

2.4 Results and Discussion

We measured the detection efficiency of the TSI 3025 CPC operated at the TWs shown in Table 1 using particles having mobility diameters from 0.94 to 4.5 nm. The temperature difference between saturator and condenser was kept constant at 32 °C, while the temperature window was varied by changing the condenser temperature from 2 to 10 °C and the saturator temperature from 34 to 44 °C (cf. Table 1). Further reduction below 2 °C was not possible due to the limited achievable temperature range of the CPC.

Figure 4 shows the measured η of the CPC using bromide ions (0.94 nm), positive TBABr particles (1.23, 1.55 and 1.71 nm), and positively charged Ni particles (2.5 to 4.5 nm). The detection efficiency clearly increased for sub-2 nm particles when the TW was shifted to lower values, whereas it remained constant for particles larger than 2.5 nm. Enhancement of η was found to increase with decreasing particle diameter. Figure 5 shows the measured n-fold increase of η versus particle size, calculated as the ratio of η measured at the lowest and highest temperature window (i.e. η at TW-2-34 divided by η at TW-10-42), as a function of particle size. Operating the CPC at the lowest temperature window resulted in a 7-fold increase of η for the 1.23 nm, a 2.5-fold increase for the 1.55 nm, and a 1.8-fold increase for the 1.74 nm particles. The largest overall increase of η was observed for the case of the bromide ion (0.94 nm), which exhibited a 35-fold increase of η at the lowest temperature window (cf. Figure 5).
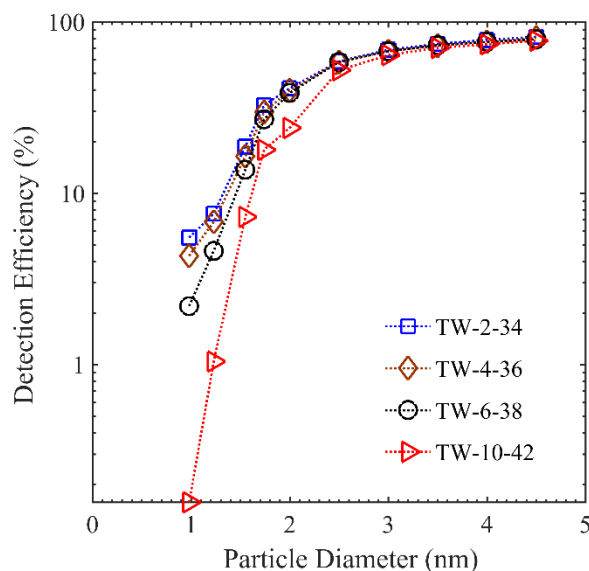
Figure 4. Measured detection efficiency of particles having sizes from 0.94 to 4.5 nm. Each data set corresponds to a different temperature window (cf. Table 1 for the nomenclature). Dashed lines are drawn to aid the eye.

It should be noted that particles of different chemical composition and polarity were used in our experiments. As shown in Figure 5, the monomer and dimer of THABr yield detection efficiency values which are larger than those of TBABr particles, even though their mobility diameters are slightly bigger. This discrepancy can be attributed to differences in the particle chemical composition, and other physical parameters such as particle solubility, affecting heterogeneous nucleation. Although the temperature window effect described here can be used to understand differences in the activation probability of particles of similar sizes but of different composition, this is beyond the scope of this work and not investigated here any further.

Having identified that the temperature window effect becomes significant for sub-2 nm particles, we calculated the detection efficiency in that particular size range using the model described above. Figure 6 shows the measured detection efficiency of the CPC using positively charged TBABr n-mer particles (with n = 1, 2, and 3) at different TWs (using the condenser temperature in the x-axis), in comparison with predictions from the simulations described in section 2. Predictions and measurements agree well at TWs located at the highest temperature investigated here, but start deviating from one another as the condenser temperature is reduced. Although the differences between measurements and predictions range from 0 to 40%, qualitatively the model predicts the increasing trend of the detection efficiency with decreasing temperature window.
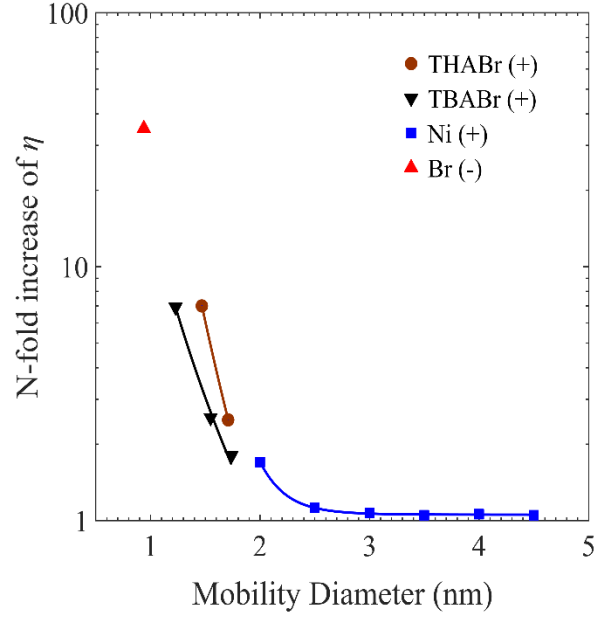
Figure 5. Measured detection efficiency of the CPC at TW-2-34, normalized with respect to measured detection efficiency at TW-10-42. The different symbols correspond to particles of different chemical composition and charge polarity. Lines represent polynomial fits through the experimental data points.

Figure 6. Measurements (symbols) and predictions (lines) of the detection efficiency corresponding to the three positive TBABr n-mers used in our experiments. The CPC was operated at a $\Delta T = 32$ °C, with the TW being varied across 5 different positions.

In order to further understand why the detection efficiency increases at lower TWs, in the discussion that follows we investigate the supersaturation profile within the condenser tube. Figure 7a shows the supersaturation value along the centerline of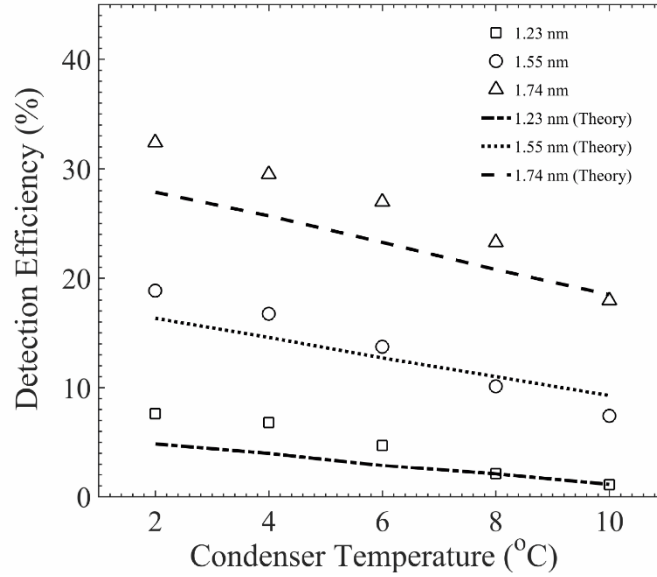 the condenser tube for three different temperature windows (TW-8-40, TW-9-41 and TW-10-42). The peak value of supersaturation increases as the TW shifts to lower temperatures. Following equation 4, higher supersaturation values lower the Gibbs free energy barrier, yielding higher activation probability. On the other hand, lower temperature would decrease the Tln(S) product resulting in the opposite effect. Figure 7b shows the calculated value of the Tln(S) for the full range of TWs used in this study. The counterbalancing effect of the lower temperature was found to be negligible. As a result, larger fraction of the sampled particles that traverse the condenser tube from the centerline will be activated at lower TWs.

Figure 8 shows activation contours of 1.23 nm particles inside the condenser tube at three different temperature windows. The contours indicate the position at which the supersaturation has the critical value for the activation of these particles. The y-axis indicates the radial position while the x-axis indicates the axial distance along the centerline of the condenser tube. The condenser inlet is located at zero axial distance while the outlet at 8.8 cm. It is apparent that the contour area is larger for the case of TW-2-34 compared to the two other cases. Going from TW-2-34 to TW-10-42 results in a 5-fold increase of the surface area under the activation line. Assuming that the particle trajectories are not significantly influenced by the absolute temperature of the condenser, more particles will transverse the activation area in the case of the lowest temperature window settings. In addition, the activation contour for TW-2-34 is extended with respect to the axial distance compared to the TW-10-42 contour. As a result, the residence time of particles inside the growth zone is increased, leading to an increase of the detection efficiency of the CPC.

Operating the CPC at different temperature windows may prove very useful in cases where the CPC is operated in scanning temperature mode (Kangasluoma et al., 2015b; Kangasluoma et al., 2015c). Gallar et al. (2006) and more recently Wang et al. (2015), have shown that it is possible to extract information of the size of the sampled particles by scanning the ΔT of the CPC. This effectively shifts the detection efficiency curve to large particle and thus information of particle size can be obtained by comparing differences in the concentration measurements at the different operating conditions. Scanning ΔT is usually achieved by increasing or decreasing the temperature of the saturator or the condenser.
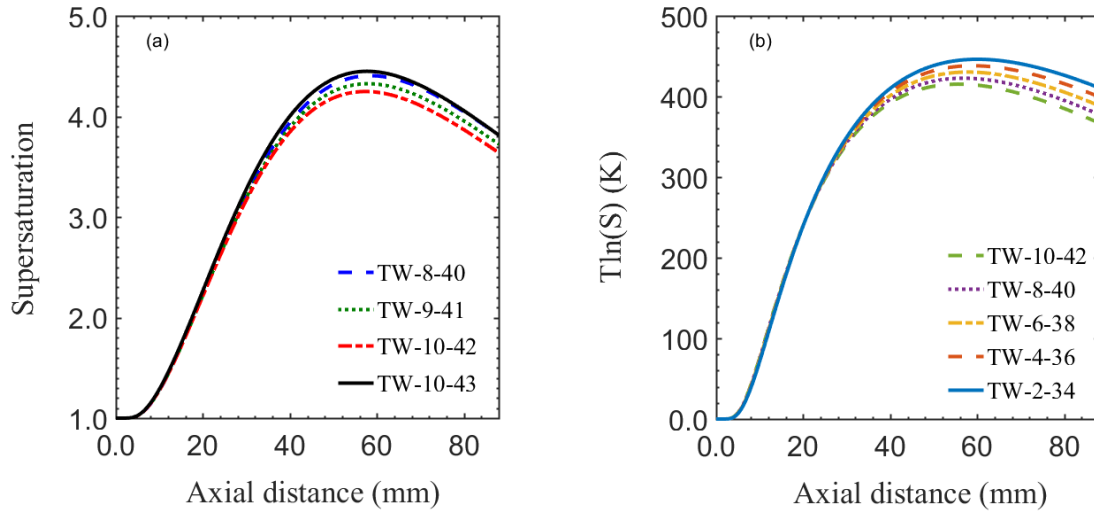
Figure 7. (a) Supersaturation profile at the centerline of the condenser tube at 3 different temperature windows with $\Delta T = 32$ °C and one temperature window with $\Delta T = 33$ °C. (b) Tln(S) product calculated at 5 different TWs with $\Delta T = 32$ °C. The x-axis represents the distance along the centerline of the condenser tube.

Considering that the temperature control resolution of the 3025 is 1 °C, the user is restricted to operating the instrument with temperature increments of 1°C, corresponding to a step in peak supersaturation. Given this limitation in temperature control, the method of scanning the TW (keeping ΔT constant) is more beneficial for sizing particles compared to scanning the ΔT. As suggested in the calculations shown in Figure 7 that were discussed above, the resulting change in the peak supersaturation value is smaller when the scanning TW mode is used (i.e. TW-8-40, TW-9-41 and TW-10-42) compared to the scanning ΔT mode (i.e. TW-10-42 and TW-10-43). The intermediate values of peak supersaturation achieved by scanning the TW can lead to higher resolving power when the CPCs are used for particle sizing.
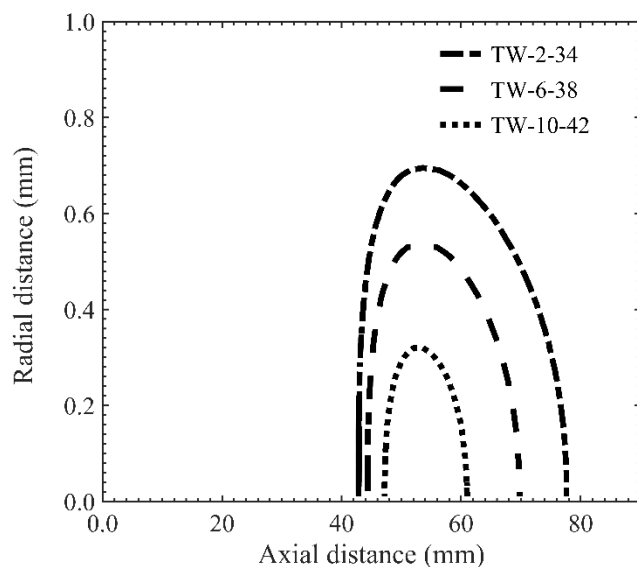
Figure 8. Activation contours corresponding to 1.23-nm particles at three different temperature windows: TW-2-34 (dash-dotted line), TW-6-38 (dashed line), and TW-10-42 (dotted line); cf. Table 1 for details of the operating conditions.

2.5 Conclusions

In this work we introduce a new controlling parameter for enhancing the detection efficiency of continuous flow CPCs. We call this parameter Temperature Window (TW), defined by the absolute value of the condenser temperature. Summarizing the key results, our investigations showed that:

- The detection efficiency of CPCs is greatly influenced not only by the temperature difference between the saturator and the condenser, but also by the absolute values of the condenser and saturator temperature. This effect is expected to influence all continuous flow CPCs operating with a working fluid whose vapor diffusion coefficient is smaller than the thermal diffusion coefficient of the carrier gas.
- A significant increase of the detection efficiency of the CPC was achieved for the sub-2 nm particles by shifting the TW to lower temperatures. The effect becomes stronger with decreasing particles size as also predicted by theory.
- By shifting the TW to lower temperatures, the peak supersaturation at the centerline is increased, while the spatial distribution of the supersaturation profile is also affected; e.g. at

low TWs the effective activation surface area is increased by a factor of 5, resulting in more particles traversing regions in the saturator where they can activate.

- As the calculations show, scanning the TW could prove beneficial compared to scanning only the ΔT when using the CPC as a particle sizer, due to the finer resolution in defining the peak supersaturation inside the condenser tube.

2.6 Supplementary Information

When particle number concentration exceeds a certain threshold value, the detection efficiency of CPCs can be reduced significantly. This is because the amount of vapor molecules condensed on the sampled particles substantially reduces the vapor concentration in the condenser, thereby restricting particles to grow to sizes suitable for optical detection. We experimentally determined the concentration threshold value by measuring the detection efficiency of the CPC using 1.47-nm particles, at various initial number concentration values (Figure S1). From this measurements we concluded that the detection efficiency did not alter significantly when using initial number concentration in the range of 10^4 to 10^3 #/cc.
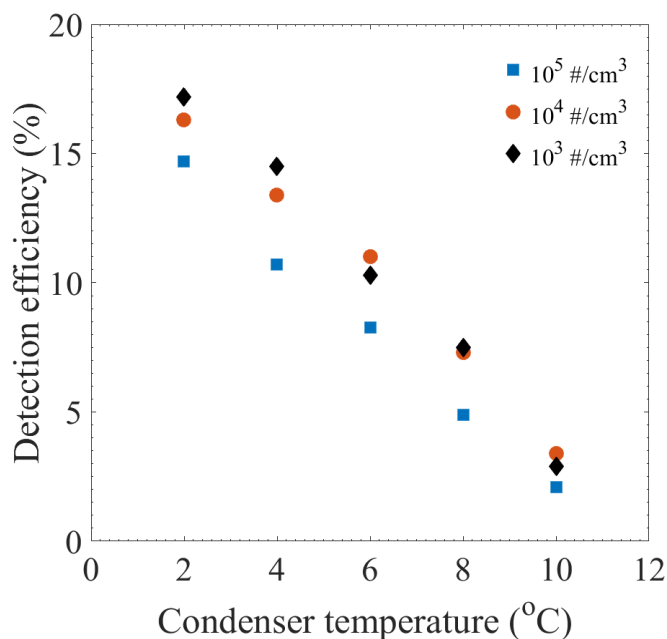

Figure S1. Measured detection efficiency of the TSI 3025 CPC using positive THABr monomer (1.47 nm) at 5 different temperature windows. Each data set corresponds to different initial particle number concentration.

References

Agarwal, J. K., & Sem, G. J. (1980). Continuous flow, single-particle-counting condensation nucleus counter. *Journal of Aerosol Science, 11*(4), 343-357.

Bricard, J., Delattre, P., Madelaine, G., & Pourprix, M. (1976). Detection of ultra-fine particles by means of a continuous flux condensation nuclei counter (pp. 566-580): Academic Press, New York.

De Juan, L., & Fernández de la Mora, J. (1998). High resolution size analysis of nanoparticles and ions: Running a Vienna DMA of near optimal length at Reynolds numbers up to 5000. *Journal of aerosol science, 29*(5), 617-626.

Dean, J. A. (1999). *Lange's Handbook of Chemistry*. New York: McGraw Hill.

Fernández de la Mora, J., de Juan, L., Eichler, T., & Rosell, J. (1998). Differential mobility analysis of molecular ions and nanometer particles. *TrAC Trends in Analytical Chemistry, 17*(6), 328-339.

Fernández de la Mora, J., & Kozlowski, J. (2013). Hand-held differential mobility analyzers of high resolution for 1–30nm particles: Design and fabrication considerations. *Journal of Aerosol Science, 57*, 45-53.

Fletcher, N. (1958). Size effect in heterogeneous nucleation. *The Journal of chemical physics, 29*(3), 572-576.

Gallar, C., Brock, C. A., Jimenez, J. L., & Simons, C. (2006). A variable supersaturation condensation particle sizer. *Aerosol science and technology, 40*(6), 431-436.

Gormley, P., & Kennedy, M. (1948). *Diffusion from a stream flowing through a cylindrical tube.* Paper presented at the Proceedings of the Royal Irish Academy. Section A: Mathematical and Physical Sciences.

Hering, S. V., Stolzenburg, M. R., Quant, F. R., Oberreit, D. R., & Keady, P. B. (2005). A laminar-flow, water-based condensation particle counter (WCPC). *Aerosol Science and Technology, 39*(7), 659-672.

Hermann, M., & Wiedensohler, A. (2001). Counting efficiency of condensation particle counters at low-pressures with illustrative data from the upper troposphere. *Journal of Aerosol Science, 32*(8), 975-991.

Iida, K., Stolzenburg, M. R., & McMurry, P. H. (2009). Effect of working fluid on sub-2 nm particle detection with a laminar flow ultrafine condensation particle counter. *Aerosol Science and Technology, 43*(1), 81-96.

Kangasluoma, J., Ahonen, L., Attoui, M., Vuollekoski, H., Kulmala, M., & Petäjä, T. (2015a). Sub-3 nm Particle Detection with Commercial TSI 3772 and Airmodus A20 Fine Condensation Particle Counters. *Aerosol Science and Technology, 49*(8), 674-681.

Kangasluoma,J.,Attoui,M.,Junninen,H.,Lehtipalo,K.,Samodurov,A.,Korhonen,F.,Sarnela,N.,Schmidt-Ott,A.,Worsnop,D.,Kulmala,M.,Petaja,T. (2015b). Sizing of neutral sub 3nm tungsten oxide clusters using Airmodus Particle Size Magnifier. *Journal of Aerosol Science, 87,53-62*

Kangasluoma,J.,Franchin,A.,Duplissy,J.,Ahonen,L.,Korhonen,F.,Attoui,M.,Mikkila,J,Lehtipalo,K.,Vanhannen,J.,Kulmala,M.,Petaja,T.(2015c). Operation of the AIrmodus A11naono Condensation Nucleus Counter at various inlet pressures,variousoperation temperatures and design of new inlet system. *Atmospheric Measurement Techniques, 8,* 8483-8508

Kangasluoma, J., Kuang, C., Wimmer, D., Rissanen, M., Lehtipalo, K., Ehn, M., Worsnop, D., Wang, J., Kulmala, M., & Petäjä, T. (2014). Sub-3 nm particle size and composition dependent response of a nano-CPC battery. *Atmospheric Measurement Techniques, 7*(3), 689-700.

Kousaka, Y., Niida, T., Okuyama, K., & Tanaka, H. (1982). Development of a mixing type condensation nucleus counter. *Journal of Aerosol Science, 13*(3), 231-240.

Kuang, C., Chen, M., McMurry, P. H., & Wang, J. (2012). Modification of laminar flow ultrafine condensation particle counters for the enhanced detection of 1 nm condensation nuclei. *Aerosol Science and Technology, 46*(3), 309-315.

Kulmala, M., Kontkanen, J., Junninen, H., Lehtipalo, K., Manninen, H. E., Nieminen, T., Petäjä, T., Sipilä, M., Schobesberger, S., & Rantala, P. (2013). Direct observations of atmospheric aerosol nucleation. *Science, 339*(6122), 943-946.

Kulmala, M., Mordas, G., Petäjä, T., Grönholm, T., Aalto, P. P., Vehkamäki, H., Hienola, A. I., Herrmann, E., Sipilä, M., & Riipinen, I. (2007). The condensation particle counter battery (CPCB): A new tool to investigate the activation properties of nanoparticles. *Journal of aerosol science, 38*(3), 289-304.

Kulmala, M., Vehkamäki, H., Petäjä, T., Dal Maso, M., Lauri, A., Kerminen, V.-M., Birmili, W., & McMurry, P. H. (2004). Formation and growth rates of ultrafine atmospheric particles: a review of observations. *Journal of Aerosol Science, 35*(2), 143-176.

Lehtipalo, K., Sipilä, M., Riipinen, I., Nieminen, T., & Kulmala, M. (2009). Analysis of atmospheric neutral and charged molecular clusters in boreal forest using pulse-height CPC. *Atmospheric Chemistry and Physics, 9*(12), 4177-4184.

Liu, B. Y., Whitby, K. T., & Pui, D. Y. (1974). A portable electrical analyzer for size distribution measurement of submicron aerosols. *Journal of the Air Pollution Control Association, 24*(11), 1067-1072.

Magnusson, L.-E., Koropchak, J. A., Anisimov, M. P., Poznjakovskiy, V. M., & de la Mora, J. F. (2003). Correlations for vapor nucleating critical embryo parameters. *Journal of Physical and Chemical Reference Data, 32*(4), 1387-1410.

Maißer, A., Barmpounis, K., Attoui, M., Biskos, G., & Schmidt-Ott, A. (2015). Atomic Cluster Generation with an Atmospheric Pressure Spark Discharge Generator. *Aerosol Science and Technology, 49*(10), 886-894.

Maißer, A., Premnath, V., Ghosh, A., Nguyen, T. A., Attoui, M., & Hogan, C. J. (2011). Determination of gas phase protein ion densities via ion mobility analysis with charge reduction. *Physical Chemistry Chemical Physics, 13*(48), 21630-21641.

McMurry, P. H. (2000). The history of condensation nucleus counters. *Aerosol Science & Technology, 33*(4), 297-322.

Mordas, G., Kulmala, M., Petäjä, T., Aalto, P. P., Matulevicius, V., Grigoraitis, V., Ulevicius, V., Grauslys, V., Ukkonen, A., & Hämeri, K. (2005). Design and performance characteristics of a condensation particle counter UF-02proto. *Boreal environment research, 10*(6), 543-552.

Peineke, C., Attoui, M., & Schmidt-Ott, A. (2006). Using a glowing wire generator for production of charged, uniformly sized nanoparticles at high concentrations. *Journal of aerosol science, 37*(12), 1651-1661.

Rosser, S., & Fernández de la Mora, J. (2005). Vienna-type DMA of high resolution and high flow rate. *Aerosol Science and Technology, 39*(12), 1191-1200.

Rus, J., Moro, D., Sillero, J. A., Royuela, J., Casado, A., Estevez-Molinero, F., & Fernández de la Mora, J. (2010). IMS–MS studies based on coupling a differential mobility analyzer (DMA) to commercial API–MS systems. *International Journal of Mass Spectrometry, 298*(1), 30-40.

Saghafifar, H., Kürten, A., Curtius, J., von der Weiden, S.-L., Hassanzadeh, S., & Borrmann, S. (2009). Characterization of a modified expansion condensation particle counter for detection of nanometer-sized particles. *Aerosol Science and Technology, 43*(8), 767-780.

Seto, T., Okuyama, K., De Juan, L., & de la Mora, J. F. (1997). Condensation of supersaturated vapors on monovalent and divalent ions of varying size. *The Journal of chemical physics, 107*(5), 1576-1585.

Sgro, L. A., & Fernández de la Mora, J. (2004). A simple turbulent mixing CNC for charged particle detection down to 1.2 nm. *Aerosol Science and Technology, 38*(1), 1-11.

Sipilä, M., Lehtipalo, K., Attoui, M., Neitola, K., Petäjä, T., Aalto, P., O'Dowd, C., & Kulmala, M. (2009). Laboratory verification of PH-CPC's ability to monitor atmospheric sub-3 nm clusters. *Aerosol Science and Technology, 43*(2), 126-135.

Sipilä, M., Lehtipalo, K., Kulmala, M., Petäjä, T., Junninen, H., Aalto, P., Manninen, H., Kyrö, E.-M., Asmi, E., & Riipinen, I. (2008). Applicability of condensation particle counters to measure atmospheric clusters. *Atmospheric Chemistry and Physics, 8*(14), 4049-4060.

Stolzenburg, M. R., & McMurry, P. H. (1991). An ultrafine aerosol condensation nucleus counter. *Aerosol Science and Technology, 14*(1), 48-65.

Thomson, J. J. (1888). *Applications of dynamics to physics and chemistry*: Macmillan.

Ude, S., & Fernández De la Mora, J. (2005). Molecular monodisperse mobility and mass standards from electrosprays of tetra-alkyl ammonium halides. *Journal of aerosol science, 36*(10), 1224-1237.

Vanhanen, J., Mikkilä, J., Lehtipalo, K., Sipilä, M., Manninen, H., Siivola, E., Petäjä, T., & Kulmala, M. (2011). Particle size magnifier for nano-CN detection. *Aerosol Science and Technology, 45*(4), 533-542.

Wagner, P. (1985). A constant-angle Mie scattering method (CAMS) for investigation of particle formation processes. *Journal of colloid and interface science, 105*(2), 456-467.

Wang, Y., Fang, J., Attoui, M., Chadha, T. S., Wang, W.-N., & Biswas, P. (2014). Application of Half Mini DMA for sub 2nm particle size distribution measurement in an electrospray and a flame aerosol reactor. *Journal of Aerosol Science, 71*, 52-64.

Wang, Z., Su, H., Wang, X., Ma, N., Wiedensohler, A., Pöschl, U., & Cheng, Y. (2015). Scanning supersaturation condensation particle counter applied as a nano-CCN counter for size-resolved analysis of the hygroscopicity and chemical composition of nanoparticles. *Atmos. Meas. Tech., 8*(5), 2161-2172.

Chapter 3

Lightweight differential mobility analyzers:

Toward new and inexpensive manufacturing methods

3.1 Introduction

The Differential Mobility Analyzer (DMA) is the most commonly used instrument for sizing sub-micron particles suspended in gases. Numerous design variations, each of which aims toward optimizing a certain aspect of its performance such as the size range and resolution, have been proposed since the DMA was first introduced in the mid-70s (e.g., Zhang et al. 1995; Rossell-Lompart et al. 1996; de Juan and de la Mora 1998; Giamarelou et al. 2011). Despite the wide variety of DMA designs, however, little attention has been paid to other practical aspects such as their weight and manufacturing cost.

The weight of conventional DMAs is in the order of a few kg, limiting their portability and use in nanoparticle exposure studies or in airborne measurements using unmanned aerial vehicles (UAVs). What is more, their manufacturing cost is in the order of several thousand USD, which is significant, especially when a number of DMAs is needed for distributed measurements of atmospheric aerosols. Although recent efforts have led to simple and inexpensive tools for sizing aerosol particles (Bezantakos et al. 2015), using a DMA offers many advantages. An effort to reduce the manufacturing cost of DMAs was made by Mei et al. (2011) who designed and built a DMA consisting of fewer parts. By doing so, they managed to produce a DMA that costs less than 50% to build compared to the classical design, and weighs ca. 350 g (D. R. Chen 2015, personal communication).

Existing DMAs are exclusively manufactured out of metal due to the necessary electrical conductivity for establishing a well-defined electric field. Using metals as building materials, however, is the very reason of their high weight and manufacturing cost. The possibility of manufacturing DMAs out of polymers, therefore,would be highly advantageous since many simple and inexpensive techniques (e.g., room temperature molding and three-dimensional (3D) printing) are available. In addition, avoiding using metals would allow one to choose from a vastnumber of materials with significantly lower density, thereby reducing instrument weight.

Here we describe an alternative method for manufacturing DMAs using low-cost and low-density polymers to build their body, and metal coatings for providing conductivity only where needed (i.e., on the inner DMA surface). More specifically, we have built a DMA using polyurethane and spray-coated the inner surface with a 0.5-mm thick conductive Nickel film. The weight of the polyurethane DMA (referred to as the PU-DMA from this point onward) is 95% lower compared to that of its metallic counterpart, while its cost is also reduced substantially. The

performance of the PU-DMA is tested in comparison to that of an identical stainless-steel DMA (SS-DMA).

3.2. Manufacturing

The design of the PU-DMA developed in this work was based on a custom-made cylindrical SS-DMA consisting of five metallic parts (i.e., the inner and outer electrode, the aerosol entrance slit, and the inlet and outlet base; see Figure S1). To create these parts out of polyurethane we used a mold-casting process. The first step of the process was to create a mold for each part of the SS-DMA using flexible silicone rubber (see the online supplemental information [SI]). To do so, each piece was placed inside a container and liquid silicone rubber was poured until fully submerged. The metallic pieces were removed from their molds after ca. 1 h that was required for the silicone to harden. Liquid polyurethane was then poured into the mold and allowed to solidify for ca. 1 h.

In order to make the inner surfaces of the PU-DMA (i.e., those coming in contact with the sampled aerosols as indicated in Figure S1) conductive, we spray-coated them with a nickel film and allowed to dry. Three cycles of a spraying/drying process were sufficient to achieve full coverage of the surface, yielding a 0.5-mm thick conductive film on the surface of each part, as determined by profileometry. As a result of the thickness of the conductive film, the gap between the two electrodes in the PU-DMA is reduced by 1 mm compared to the SSDMA. The geometric dimensions of both DMAs used in this work are summarized in Table S1.

The weight of the resulting PU-DMA is 150 g, which is significantly lower than that of the SS-DMA (3.5 kg), while the cost of the materials used for manufacturing is ca. 100 USD. Considering that multiple DMAs can be produced from a single mold, the associated cost can be further reduced, making the proposed method highly attractive.

3.3. Characterization

The performance of the two DMAs was initially compared by using them as part of a differential mobility particle sizer (DMPS) for measuring the particle size distribution of a stable laboratory-generated polydisperse aerosol (see route 1 in Figure S2 and associated discussion in the SI). Measurements were performed at aerosol to sheath flow rate ratios b of 1.5/5.0, 1.5/7.0, and 1.5/ 10.0.

The midpoint particle electrical mobility corresponding to each potential difference applied between the two electrodes of the test DMAs was calculated as (Knutson and Whitby 1975):

$$Z^* = \frac{Q_{sh}}{2\pi VL} \ln\left(\frac{R_2}{R_1}\right)$$

[1]

where Qsh is the sheath flow rate, V is the potential difference between the two DMA electrodes, L is the distance between the polydisperse aerosol inlet and the monodisperse aerosol outlet slit, while R1 and R2 are the inner and outer electrode radii, respectively. By definition, the electrical mobility of the particles is given by (Hinds 1999):

$$Z_p = \frac{neC_c(d_m)}{3\pi\eta d_m}$$

[2]

Here n is the number of elementary charges, e is the electron charge, h is the gas viscosity, dm is the particle diameter, and Cc is the Cunningham slip correction factor given by:

$$C_c(d_m) = 1 + \frac{\lambda}{d_m}\left(2.51 + 0.8 * \exp\left(-0.55\frac{d_m}{\lambda}\right)\right)$$

[3]

where λ is the gas mean free path. In all cases, we assume that the particles carry one elementary charge. The size of the particles classified by the DMA for every set of operating conditions (i.e., potential difference between the electrodes and sheath flow rate) can be estimated by equating Equations (1) and (2) and solving iteratively. The transfer functions of both DMAs (i.e., the SS- and the PU-DMA) were measured with a tandem DMA configuration (Rader and McMurry 1986). Nearly monodisperse particles were produced by a glowing wire (GW) generator in series with a long SS-DMA (LSS-DMA; see route 2 in Figure S2). The transfer function of the tested DMA was determined by stepping their voltage across the mobility range of the monodisperse particles produced by the GW generator and the LSS-DMA. The measured signal of a tandem DMA system expressed as a ratio of the concentrations of particles at the polydisperse aerosol inlet N1 and at the monodisperse aerosol outlet N2 of the test DMA, can be determined by:

$$\frac{N_2}{N_1} = \frac{\int_0^{+\infty} \Omega_1(Z_p, Z_1)\Omega_2(Z_\pi, Z_2^*)dZ_p}{\int_0^{+\infty} \Omega_1(Z_p, Z_1^*)dZ_p}$$

[4]

Here V1 and V2 are the transfer functions corresponding to the LSS-DMA and the test DMA, respectively, whereas Z 1 is the midpoint electrical mobility (see Equation (1)) of the monodisperse aerosol particles downstream the LSS-DMA. The key parameters defining the

transfer functions of the test DMAs were determined using the tandem DMA measurements and the deconvolution scheme described by Stratmann et al. (1997).

3.4 Results and discussion

Figure 1 shows the normalized concentration of the charged tungsten particles (produced by the GW generator) measured by the PU- or the SS-DMA when set at different voltages and at b D 1.5/5.0. Log-normal curves were fitted to the data using a nonlinear least-square method. The mean particle size determined by the measurements using the PU-DMA was in excellent agreement with those using the SS-DMA. The total number concentration measured by the PU-DMA, however, was found to be6 lower compared to that measured by the SS-DMA.
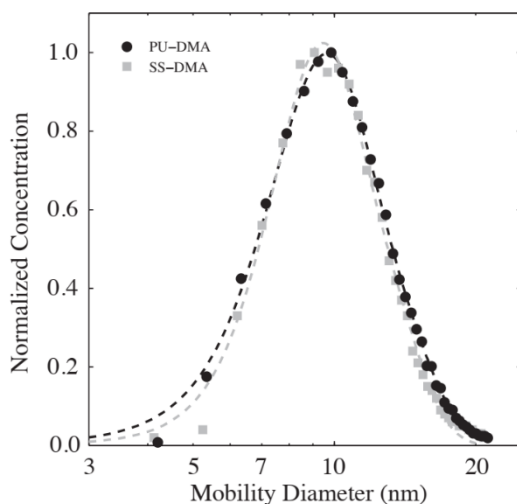

Figure 1. Size distribution measurements of polydisperse charged tungsten nanoparticles measured using either the PU-DMA (circles) or the SS-DMA (squares) at an aerosol to sheath flow ratio of 1.5/7.0.

When the sheath flow rate through the two DMAs was increased to 7.0 (b D 1.5/7.0) and 10.0 lpm (b D 1.5/10.0), the difference between the mean particle mobility diameter measured by the two classifiers increased to 2.9 and 8.9%, respectively (see Figure S3). We attribute this difference to structural non-idealities of the PU-DMA, which can cause small flow disturbances closeto the electrode walls and thus to the trajectories of the particles as the flow rate through the classifier increases. Such non-idealities can originate from surface defects (e.g., variability of the coating thickness), or from misalignment of the inner electrode, which in turn can cause non-idealities in the electric and flow fields that would require numerical models to evaluate them.

Figure2 compares measured and predicted (using Equation (4)) N2/N1 ratios for 10-nm monodisperse particles when either the PU- or the SS-DMA were used in the tandem DMA system. The height and full width at half maximum (FWHM) of the transfer functions of both DMAs determined by these measurements and the deconvolution scheme described by Stratmann et al. (1997) are shown in Figure S4. Although the height and FWHM of the transfer functions of both DMAs as a function of particle size follow the same trend with the theory, the PU-DMA exhibits larger deviations compared to the SS-DMA. These deviations can be explained by small geometrical differences between the two DMAs that cannot be captured by Equation (4). The 0.5-mm thick coating, for instance, reduces the gap of every channel in the DMA, with the most sever being that of the aerosol inlet slit, which narrows down to half the size of that of the SS-DMA. This can lead to pronounced aerosol recirculation affecting the performance of the PU-DMA (Chen et al. 1999). To fully capture that, however, a particle-trajectory model would be required, which is out of the scope of the current study.
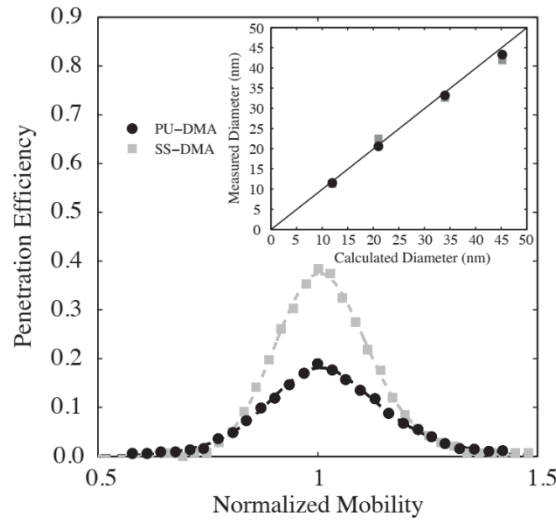
Figure 2. Predicted (line) and measured response of the tandem DMA system using either the PU-DMA (circles) or the SS-DMA (squares) determined using 10 nm particles. Inset shows the correlation between measured and calculated midpoint mobility diameter. For both DMAs.

The inset of Figure 2 shows the mean mobility diameter measured by the test DMAs versus the midpoint mobility diameter calculated by Equations (1) and (2) using the dimensions provided in Table S2. Evidently agreement for these specific operating conditions (b D 1.5/5.0) is well within a 3% experimental uncertainty that is typical for DMAs (Kinney et al. 1991), showing that the PU-DMA performs equally well compared to the SS-DMA in this respect. Repeated measurements over a period of 6 months showed similar performance, indicating that the PU-DMA is also durable.

3.5 Conclusions

In this work, we introduce a new method for manufacturing DMAs with extremely small weight and low manufacturing cost. We do so by avoiding using metals as building material, which has been the common practice thus far. Instead, we use parts made of a polymer that are coated with a conductive film. We prove this concept by constructing a DMA out of polyurethane, achieving more than 95% reduction in weight and a significant decrease in manufacturing cost. The performance of this DMA (i.e., the PU-DMA) was evaluated in comparison to an identical metallic DMA made of stainless steel (i.e., the SSDMA). The measurements performed with the PU-DMA show good overall agreement with the ones performed with the SS-DMA, providing confidence in using it for routine particle mobility measurements. Differences between the measured mean size of particles from a polydisperse aerosol using the PU- and the SS-DMA was within experimental uncertainty when low sheath flow rate (i.e., 5.0 lpm) was used through the classifiers, but increased up to 8.9% for higher flows. These quantitative differences are attributed to manufacturing uncertainties of the PU-DMA.

Despite these differences, the performance of the PU-DMA manufactured with the method described in this work is encouraging, providing a first step toward the development of cost-effective lightweight instruments. An upgrade of this method, in terms of manufacturing precision, can involve the use of 3D printing technology for building DMA bodies out of a number of polymers. Doing so will offer the possibility of improving the accuracy and precision of the classifiers and further reducing their production costs.

Funding

3.6 Supplementary Information

S1. Manufacturing materials and procedure

The polyurethane DMA (PU-DMA) described in them main manuscript was manufactured with a mold casting production process, using silicone rubber as molding material. Silicone rubber of low flexibility (PS 8530 by Poly-Service BV) was found to be beneficial for molding all the DMA pieces (i.e., the inner and outer electrode, the aerosol entrance slit, and the inlet and outlet base). Due to its low flexibility, this type of rubber provides structural support to the mold and avoids bending due to its own weight, which in turn can cause misalignment problems between the inner with the outer electrode. A high flexibility silicone rubber (PS 8510 by Poly-Service BV) was found to be more practical for making molds of the smaller pieces that require higher accuracy. The PU-DMA body parts were then cast out of the prepared molds. We used a twocomponent liquid polyurethane (PU H 70 by Poly-Service BV), which solidifies after casting. The density of polyurethane is 0.07 g/cm3. In order to make the PU-DMA parts conductive, their inner surface was spray-coated with an electrically conductive material based on nickel powder (ENSCP400H by Electrolube). The nominal resistivity of the material ranges from 0.3 to 0.7 Ohm/sq. for 50-μm thick films.

S2. Experimental setup and procedure

Figure S1 (route 1) shows the experimental setup employed for measuring polydisperse aerosol size distributions using the test DMAs. Polydisperse tungsten nanoparticles were produced by a glowing wire (GW) generator (Peineke et al., 2006), operated with a N2 flow of 3 lpm. The polydisperse aerosol was subsequently passed through a 241Am neutralizer (Vivas et al., 2008) in order to establish an equilibrium charge distribution on the particles. The charged particles were then classified by the test DMA (i.e., either the PU- or the stainless-steel DMA; SS-DMA), and subsequently their concentration was measured by a condensation particle counter (CPC, TSI 3025A). Measurements were performed with aerosol to sheath flow rate ratios β of 1.5/5.0, 1.5/7.0 and 1.5/10.0. The sheath flow rate in both DMAs was controlled by closed loop flow systems (cf. Biskos et al. 2006).   Both DMAs were operated in stepping voltage mode, while the particle concentration at their monodisperse aerosol outlets was measured by the CPC. After the completion of one mobility distribution measurement, the DMAs were switched and the measurement was

repeated. The reported size distributions are the average of three independent measurements using each DMA.

Figure S1 (route 2) shows the tandem DMA configuration (TDMA; Hummes et al. 1996) used to measure the penetration efficiency for particles having different diameters. A cylindrical custom-made long stainless steel DMA (LSS-DMA; cf. Table S1 for its dimensions) was used as a first DMA in the setup. The LSS-DMA was operated at fixed voltages for selecting particles within a narrow size/mobility range (i.e., near monodisperse aerosol) at an aerosol to sheath flow ratio of 1.5/8.0. The resulting monodisperse aerosol flow was then measured upstream and downstream the test DMA (in order to determine N1 and N2 in Eq.2, respectively), which was operated at a stepping voltage mode.
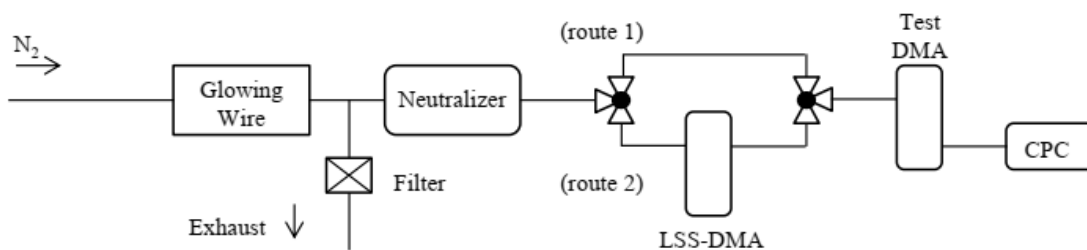
Figure S1. Schematic layout of the experimental setup employed for characterizing the PU- and SS-DMA using polydisperse (route 1) and monodisperse (route 2) aerosol particles.

Table S1. Characteristic dimensions of the DMAs used in this study.

	Effective Length (cm)	Outer Electrode Diameter (cm)	Inner Electrode Diameter (cm)
SS-DMA	11.4	1.954	0.935
PU-DMA	11.4	2.004	0.985
LSS-DMA	44.3	1.954	0.935

S3. Measured penetration efficiency at higher flow rates

Figure S2. Size distribution measurements of tungsten polydisperse aerosol nanoparticles measured using either the PU-DMA (circles) or the SS-DMA (squares) at an aerosol to sheath flow ratio of 1.5/7.0 (a) and 1.5/10 (b).

Figure S3. Measured penetration efficiencies of monodisperse aerosol particles, having sizes from 10 to 40 nm, through the PU- and SS-DMA operated at an aerosol to sheath ratio of 1.5/7.0.

References
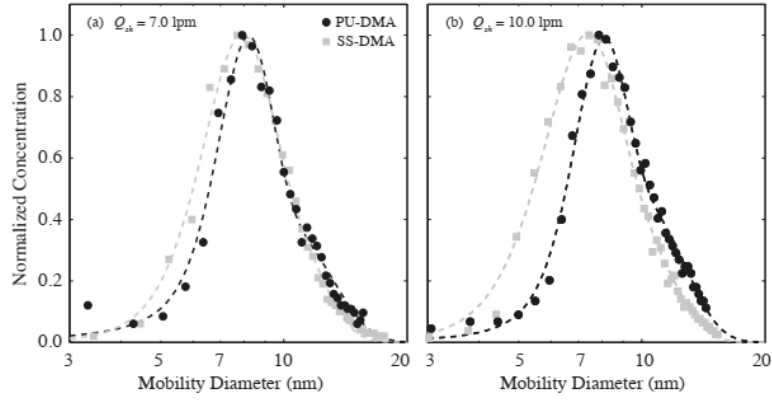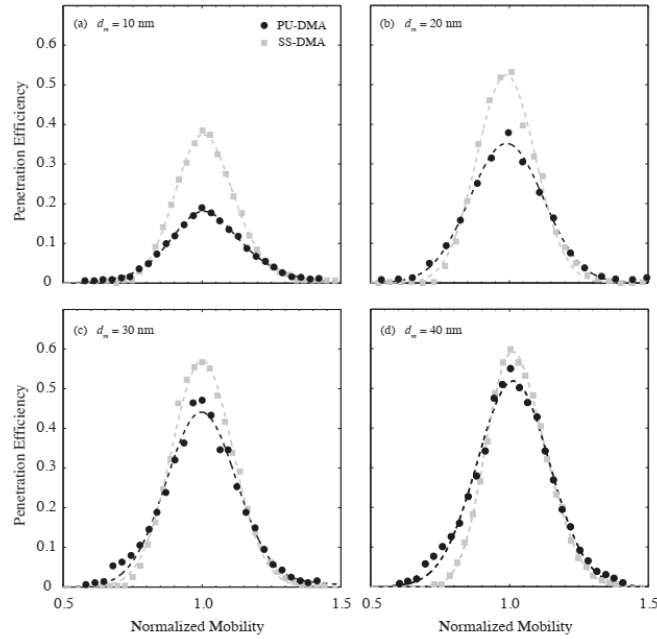
Bezantakos, S., Huang, L., Barmpounis, K., Attoui, M., Schmidt-Ott, A., and Biskos, G. (2015). A Cost-Effective Electrostatic Precipitator for Aerosol Nanoparticle Segregation. Aerosol Sci. Technol., 49:IV–VI.

de Juan, L., and de la Mora, J. F. (1998). High Resolution Size Analysis of Nanoparticles and Ions: Running a Vienna DMA of Near Optimal Length at Reynolds Numbers up to 5000. J. Aerosol Sci., 29:617 –626.

Chen, D.-R., Pui, D. Y. H., Mulholland, G. W., and Fernandez. M., (1999). Design and Testing of an Aerosol/Sheath Inlet for High Resolution Measurements with a DMA. J. Aerosol Sci., 30(8):983–999.

Giamarelou, M., Stolzenburg, M., and Biskos, G. (2011). The Multiple Monodisperse Outlet Differential Mobility Analyzer: Derivation of Its Transfer Function and Resolution. Aerosol Sci. Technol., 46:951–965.

Hinds, W. C. (1999). Aerosol Technology: Properties, Behavior, and Measurement of Airborne Particles, 2nd Ed. John Wiley & Sons, Inc., New York.

Kinney, P. K., Pui, D. Y. H., Mulholland, G. W., and Bryner, N. P. (1991). Use of the Electrostatic Classification Method to Size 0.1-mm SRM Particles—A Feasibility Study. J. Res. Natl. Inst. Stand. Technol., 96(2):147–176.

Knutson, E. O., and Whitby, K. T. (1975). Aerosol Classification by Electric Mobility: Apparatus, Theory, and Applications. J. Aerosol Sci., 6:443–451.

Mei, F., Huijing, F., and Chen, D. R. (2011). A CostEffective Differential Mobility Analyzer (cDMA) for Multiple DMA Column Applications. J. Aerosol Sci., 42:462–473.

Rader, D. J., and McMurry, P. H. (1986). Application of the Tandem Differential Mobility Analyzer to Studies of Droplet Growth or Evaporation. J. Aerosol Sci., 17:771 –787.

Rossell-Lompart, J., Loscertales, T. G., Bingham, D., and de la Mora, J. F. (1996). Sizing Nanoparticles and Ions with a Short Differential Mobility Analyzer. J. Aerosol Sci., 27:695–720.

Stratmann, F., Kauffeldt, Th., Hummes, D., and Fissan, H. (1997). Differential Electrical Mobility Analysis: A Theoretical Study. Aerosol Sci. Technol., 26:368–383.

Zhang, S.-H., Aksutsu, Y., Russel, L. M., Flagan, R. C., and Seinfeld, J. H. (1995). Radial Differential Mobility Analyzer. Aerosol Sci. Technol., 23:357–372.

Chapter 4

Atomic Cluster Generation with an Atmospheric Pressure Spark Discharge Generator

Abstract

A new method for generating metal clusters in the gas phase is described and characterized in this work. The method is based on material evaporation by spark ablation, at atmospheric pressure. The characterization of atomic clusters was done by measuring their electrical mobility. The measured mobilities were compared with values found in literature in order to identify the cluster species. We show that silver clusters consisting from one up to 25 atoms can be produced in helium at atmospheric pressure. In addition, the effect of oxygen concentration on the resulting cluster mobility distribution was investigated. Results show that at higher oxygen level, the mobility distribution is dominated by the abundance of stable clusters (i.e. magic number clusters). This can be attributed to an oxidation etching effect.

4.1 Introduction

The need for nanoparticle production in various fields of science and technology has been growing significantly over the past decades. Because of their large surface to volume ratio compared to bulk material, nanoparticles show special properties different from the bulk materials. These properties are related to quantum mechanic size effects or surface effects. Such properties are e.g. lower melting points, higher solid-solid phase transition pressure, thermophysical properties or size-dependent catalytic activity (Kruis et al. 1998). Because of these properties nanoparticles find application in the fields of sensors (Leite et al. 2000; Luo et al. 2006), solar cell technology (Subramanian et al. 2001), functional textiles (Perelshtein et al. 2008), but also in medicine for e.g cancer treatment (Cho et al. 2008) etc. Nanoparticles are also important for environmental processes that play a major role in particle formation in the atmosphere and thus subsequently affect cloud formation and climate (Kulmala et al. 2004; Wang et al. 2010).

On the lower end of the nanoparticle size range, particles are often referred to as clusters and consist only of a small number of atoms n (i.e. < 100/cluster). While the specific properties of nanoparticles can be typically scaled with size, the physicochemical properties of atomic clusters are related to the number of valence electrons. The valence electrons form electronic shells just like atoms which led to the introduction of the term "superatoms", when referring to atomic clusters that exhibit similar properties with those of other elements of the periodic table (Jena 2013; Khanna and Jena 1995). Cluster assembled materials as well as catalysts (Claridge et al. 2009) tailored to specific applications clearly appear possible.

Several different approaches for nanoparticle production have been developed in the past, but most of these techniques carry certain limitations when trying to extend their sizes to the range of atomic clusters. Mechanical milling processes require high energies if aiming for particle sizes below 20 nm. Conventional wet chemistry methods require the use of solvents and surfactants which are sources for contaminations. Physical aerosol-based methods (i.e. evaporation/condensation) such as tube furnace, have been proven to be very useful for nanoparticle generation. In this method material placed in a heated crucible is evaporated and subsequently cooled to generate airborne nanosized particles (Scheibel 1983). Heating in this method, however, is not only restricted to the material of interest but also to the rest of the ceramic tube. This introduces a source of contamination which is difficult to control and is a significant limitation to the production of high purity nanoparticles (Kruis et al. 1998). Flame synthesis techniques using a range of precursor solutions (Pratsinis 1998; Wang et al. 2014; Zhang et al.

2012) have been recently used to produce high concentration of stable clusters in the sub-2-nm size range. Due to the presence of O_2 in flame synthesis reactors, however, these methods yield into highly oxygenated clusters (Fang et al. 2014).

Atomic clusters for fundamental research are typically generated via pulsed laser ablation where the energy of a laser is used to locally heat up and thus evaporate material (Bondybey and English 1982; de Heer 1993). Because of the very localized heating, laser ablation offers a high degree of control over contaminations that leads to high surface purity (Ullmann et al. 2002). This technique works over a wide range of nanoparticle sizes and is especially suited for generation of small atomic clusters. However, mainly due to high cost and safety issues associated to the work with a laser, the method is not widespread for applications in aerosol research.

A different method, which carries the potential of being used as a cluster generation source, is spark ablation or also called spark discharge generation (SDG), introduced by Schwyn et al. (1988). The particle formation process in SDG is similar to that of laser ablation. The ion cloud of evaporated material is small, compared to other evaporation-condensation processes (e.g. using a tube furnace). The initial cooling is governed mostly by adiabatic expansion and radiation and thus, cooling down to temperatures below the boiling point is relatively fast. These characteristics make the SDG method suitable for the generation of very small particles (Tabrizi et al. 2009). Since the SDG operation is based on localized heating of the material, it offers good control over contamination of the produced nanoparticles.

In this work we describe how the use of atmospheric pressure spark ablation can be extended to the generation of atomic clusters, preserving the advantages of the technique in terms of versatility, energy efficiency and controllable sources of contaminants. This approach allows atmospheric pressure at all stages: generation, classification/manipulation and detection. We report mobility measurements of positive and negative silver clusters composed of one to 25 atoms. In addition, we show how the operating parameters of the SDG technique can be used to tune the size of the produced clusters and how reaction with oxygen can influence the resulting cluster distribution.

4.2 Experimental procedure and methodology

Spark Discharge Generation (SDG)

The SDG operation is based on controlled electrical discharges between two electrodes. Localized heating of the electrodes leads to evaporation and subsequent homogeneous condensation of electrode material in a noble gas at atmospheric pressure. Figure 1 shows the layout of the experimental setup. The electrical circuit we used in the SDG is equivalent to a simple RLC circuit where a high voltage capacitor, placed in parallel to the gap between two sparking electrodes, is charged by a constant current source. When the applied voltage on the capacitor exceeds the breakdown voltage of the carrier gas, the capacitor is discharged, within about 1 µs, over the gap. As a result, a conductive channel (plasma) is formed between the electrode pair. The temperature rises locally to tens of thousand degrees Kelvin leading to evaporation of electrode material. An inert gas flow is used for dilution and cooling of the vapor cloud.

The electrical energy E dissipated in the gap between the two electrodes is given by:

$$E = \frac{1}{2}CV_d^2 \, , \tag{1}$$

where C is the capacitance and V_d the discharge voltage. The capacitor is charged after every breakdown, and the process repeats at a certain frequency that depends on current and capacitance.

The spark chamber used in this work was a standard 5-way cross (type KF NW40, vacuum flange, Hositrad Inc.). Two opposite ends were used as the gas inlet and outlet. The two electrodes were placed on the other pair of opposite ends, while the fifth end, covered by a glass window, was used as a view port for observing the spark gap. The capacitor was charged by a constant current supplied by a high voltage power supply (Technix Inc., Creteil, France). A micrometer screw was mounted on the grounded electrode for adjusting the gap distance. All the electrodes were purchased from Goodfellow (Goodfellow Inc., Pennsylvania, USA) with a purity of $\geq$ 99.997%. For our purpose of cluster generation a rod – wire configuration was applied. The diameters for the rod and the wire electrodes were 3 mm and 1 mm, respectively.
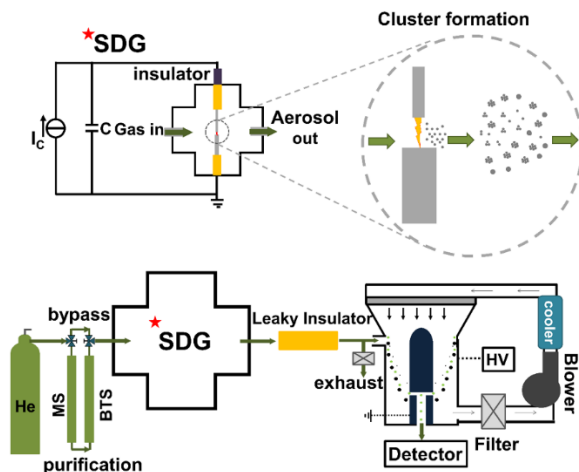
Figure 1. Schematic of the system for cluster formation by SDG: **(top left)** the electrical circuit and the spark housing, I_C is the constant current to charge the capacitor C; **(top right)** magnified region between the two electrodes showing a cartoon of the particle formation process; **(bottom)** the schematic diagram showing the experimental setup consisting of: a high-purity helium flow supplied by a gas cylinder and two purification units that can optionally be bypassed, the SDG device for cluster generation, and a differential mobility analyzer (DMA) for sizing. The DMA was operated with a recirculating sheath flow system consisting of a low pressure-drop filter, a blower and a cooler. The outer electrode of the DMA was on high voltage (HV) while the inner electrode was grounded. Two detectors were used in parallel for number concentration measurements: an aerosol electrometer (AEM) and an ultrafine condensation particle counter (uCPC).

The carrier gas (99.999% purity; $H_2O \leq 3$ppm; $O_2 \leq 2$ppm) was provided by a gas cylinder (Linde Inc., Benelux). Additional purification of the carrier gas was employed upstream of the SDG chamber, for further reduction of water and O_2 traces down to the ppb levels. The purification system consisted of an aluminosilicate (4 Å, Sigma Aldrich Inc., St. Louis, USA) molecular sieve for water removal, and of a copper-based catalyst (BASF R3-11 BTS catalyst) for oxygen removal. Both systems were placed in 50-cm long ISO-KF NW40 tubes, and were regenerated before the measurements (Vons 2010). The purification system could also be bypassed to investigate the effect of gas purity on the generated clusters (cf. Figure 1).

SDG operation for cluster generation

Due to its low breakdown voltage, which in turn requires a low energy per spark, helium is the most suited gas for cluster generation. Thus, all the results presented in this paper are for measurements in helium. The mean size of the particles produced by the SDG can be controlled by the energy per spark, the repetition frequency (Tabrizi et al. 2009), and the flow rate of the

carrier gas. The energy per spark for cluster generation in helium was determined by initial experimental testing and was in the range from 5 to about 300 µJ. These energies are 2 to 3 orders of magnitude lower compared to SDG operation for nanoparticle production in nitrogen and were achieved by operating the SDG at low capacitance and low breakdown voltage than compared to most previously published studies (Meuller et al. 2012; Tabrizi et al. 2009). The breakdown voltage can be controlled by the gap distance between the electrodes. In this work the capacitance varied between 0.125 and 5 nF, and the gap distance was kept constant at 0.7 ±0.1 mm for all measurements. The discharge voltage was measured using a voltage divider and an oscilloscope, was in the order of a few hundred volts for all measurements. The flows used were varied between 10 and 15 lpm.

It has been shown in previous studies that the electrode configuration in SDG affects the final nanoparticle structure and size. Rod-rod SDG generated nanoparticles tend to agglomerate. Agglomeration can be prevented to some extent by high dilution rates (Schwyn et al. 1988; Tabrizi et al. 2009). In a recent study (Han et al. 2012) it has been found that a pin-to-plate configuration generates smaller and less agglomerated particles at identical dilution flows. Through initial testing, we observed that a rod opposite to a wire electrode (similar to a pin to plate configuration) led to the production of stable concentration of clusters. Considering the benefits of the rod-wire combination, we used this configuration for all the measurements reported in this work. The wire was grounded and the rod was on high negative voltage. In this way, most of the material evaporates from the rod electrode (Tabrizi et al. 2009).

It has been shown for nanoparticles that the main fraction of generated clusters is neutral and only a small fraction is positively or negatively self-charged (Meuller et al. 2012; Tabrizi et al. 2009). Thus, it is safe to assume that only clusters with a single positive or negative charge are produced by the SDG, as the charging probability of multiply charged sub-2 nm clusters is extremely low (Fuchs 1963; Wiedensohler 1988). Clusters acquire their charge in the spark region, as they co-exist with electrons and helium cations produced by the spark. Another possible ionization mechanism is the UV radiation emitted from the spark, which may ionize atoms and clusters by photoemission. Initial tests showed that the number of positively charged clusters exceeded the number of negatively charged clusters in all possible electrode configurations (rod-rod, wire rod, with all polarity and grounding options). For the rod-wire configuration, the number concentration of positively charged clusters was about one order of magnitude higher compared to negatively charged clusters. This is in agreement to the results reported by Fang et al. (2014) for flame synthesized TiO_2 and SiO_2 clusters. The predominance of positive clusters can be partially

explained by the fact that metal cations are more stable than metal anions (Fernández et al. 2004). Another possible explanation is the expected dominance of positive charges in the condensing cloud of atoms produced by the evaporation of the electrodes at each spark. This is a result from the fact that they are not scavenged by the high electric field as easily as the negatively charged carrier, i.e., the electrons (electrons have a much higher diffusion coefficient and electrical mobility than the positive charge carriers). This is in agreement with findings of previous studies (Moini and Eyler 1988)

Mobility measurement and detection – Differential mobility analyzer (DMA)

A differential mobility analyzer (DMA; (Hewitt 1957; Knutson and Whitby 1975)), coupled with an aerosol electrometer (AEM) and an ultrafine condensation particle counter (uCPC) (Whitby and Clark 1966) in parallel was used to measure the mobility distribution of the clusters. The cluster laden gas flow is introduced close to the outer electrode of the DMA to merge with a laminar sheath flow. An electrical field is applied between the outer and inner electrode of the DMA, resulting in the migration of the charged clusters towards the inner electrode. Clusters having electrical mobilities within a very narrow range exit through the monodisperse outlet slit located downstream on the inner electrode, and are directed to the detector to be counted. The mobility distributions of the sampled clusters can be measured by scanning over a range of voltages.

While DMAs have been designed originally for particles in the size range of 10 to several hundreds of nanometers (Chen et al. 1996; Knutson and Whitby 1975; Reischl 1991), the DMA used in this study (half mini DMA, NanoEngineering Inc.) has been designed to enable mobility measurements of clusters and ions down to sub-nanometer sizes (Attoui et al. 2013; De Juan and Fernández de la Mora 1998; de la Mora and Kozlowski 2013; Maißer et al. 2011; Wang et al. 2014). The design of the half-mini DMA allows use of sheath flow rates of several hundreds of liters per minute that get sonic at values > 700 lpm for air. More details on the operation of high-flow DMAs can be found elsewhere (Rosser and De La Mora 2005; Steiner et al. 2010; Ude and De la Mora 2005). High-flow DMAs require calibration because of inherent difficulties of sheath flow measurements at high flow rates. To establish a mobility scale, the measurement of only one mobility standard is required. For a constant flow velocity the relationship between inverse mobility Z^{-1} and DMA V voltage is given by:

$$Z^{-1} = const \cdot V .$$
(2)

Calibration was done by electrospraying tetraheptyl ammonium bromide (THABr) using a home-made electrospray ionization (ESI) source similar to the one used by Ude and Fernandez de la Mora (Ude and De la Mora 2005). THABr salt (Sigma Aldrich, Inc., MO, USA) was diluted in acetonitrile (HPLC, ≥99.9%, Sigma Aldrich, Inc., MO, USA) to produce a solution with concentration in the range of a few tens mmol/l. The electrospraying and the mobility measurements in the DMA were conducted in in pure helium. The mobility of the resulting bromide ion (Br^-) in helium is 18.8 cm^2/Vs (Dotan and Albritton 1977).

The resolving power R of the DMA is given by $R=V_o$/FWHM, where V_o is the peak position and FWHM is the full width of the half maximum of the peak. In our case R was in the range between 15 and 20 for all measurements and has been determined by measuring size distribution of monomobile, positively charged THABr monomer and dimer ions (Ude and De la Mora 2005) in helium.

The measured electrical mobilities strongly depend on the gas composition in the DMA. Particle mobility is related to the collisions of a particle (ion cluster in our case) with neutral gas molecules. The nature of the collision, and therefore the measured mobility depends upon the gas molecule size and mass, the ion size and other possible interactions caused e.g. by the polarizability of the gas (Larriba-Andaluz et al. 2015; Tammet 1995). Before starting the measurements in helium, the DMA and the closed loop for sheath flow contained air. Because helium gas was introduced only through the DMA inlet, to ensure that the closed loop the sheath flow was filled completely with the gas, we performed a number of mobility measurements before starting to record the data. The position of the measured peaks during these first measurements shifted with respect to the DMA voltage as a result of the decreasing level of air inside the loop. After a certain amount of time, depending on the helium flow rate, the peak voltage of the clusters stabilized indicating completed gas exchange. This gave a good control over the state of helium concentration inside the DMA. Figure 2 shows the differences in mobility of $THABr^+$ in helium and nitrogen. The bottom x-axis in this graph shows inverse mobility of the clusters and the top x-axis shows the voltage (kV) applied at the DMA. It can be seen that the mobility shifts roughly by an order of magnitude.

In our measurements, the outer electrode of the DMA was on high voltage while the inner electrode was grounded. This has been found to increase transmission through the instrument due to the absence of a potential difference between the monodisperse outlet of the DMA and the grounded detector, and therefore significant minimization of electrophoretic losses (Martinez-Lozano et al. 2006). Keeping the outer electrode of the DMA on high potential, however, means

that its aerosol inlet is also at high potential. Considering that the housing of the spark chamber needs to be grounded in our configuration, there is a potential difference between the spark and the DMA inlet. To electrically insulate the spark chamber from the aerosol inlet, an electrostatic dissipative polymer (leaky insulator) tube of 4 mm inner diameter (Ensital SD, a natural copolymer acetal) was used to connect the SDG with the DMA. This material allows gradually varying the potential difference from one side of the tube to the other. In addition, electrophoretic losses of charged particles are significantly reduced by using this material, compared to those of a perfect insulating material (Martinez-Lozano et al. 2006). The flow rate through the leaky insulating tube was kept high in order to minimize the residence time and thus the cluster losses in the tube. The flow rate of the exhaust line, located just before the aerosol inlet of the DMA, was controlled by a needle valve in order to keep the aerosol flow through the classifier independent of the flow in the spark. The flow rate used through the spark chamber varied between 10 to 15 lpm while the aerosol flow in the DMA was kept at 5 lpm. The sheath flow rate in the DMA was adjusted in the order of several hundred lpm using a brushless motor blower (Domel Inc., Slovenia). All measurements presented in this study were performed using a recirculating sheath flow system at atmospheric pressure.

Particles were detected by a custom-made Faraday cup aerosol electrometer (Whitby and Clark 1966) and a commercial butanol based ultrafine condensation particle counter (CPC; TSI Model 3025). In the CPC, particles are exposed to a supersaturated environment where vapor (n-butanol) condenses on the clusters leading them to grow into sizes that are optically detectable. The CPC was operated with optimized temperature difference ΔT between the saturator and the condenser tube for helium. To find the appropriate ΔT we followed the procedure described by Kuang et al. (2012) who used the commercial butanol-based CPC (TSI Model 3025) for detecting of 1-nm sized particles. Because of the higher ratio between thermal diffusivity and mass diffusivity of butanol in helium, compared to air, a lower ΔT is needed to achieve the same supersaturation compared to air (Brus et al. 2005). In our case ΔT was set to 27 ºC, compared to 34 ºC that was used by Kuang et al. (2012). The CPC flow rates were calibrated for operation in helium. These settings led to a suitable butanol supersaturation level inside the condenser, enabling cluster detection down to the sub-nanometer range.
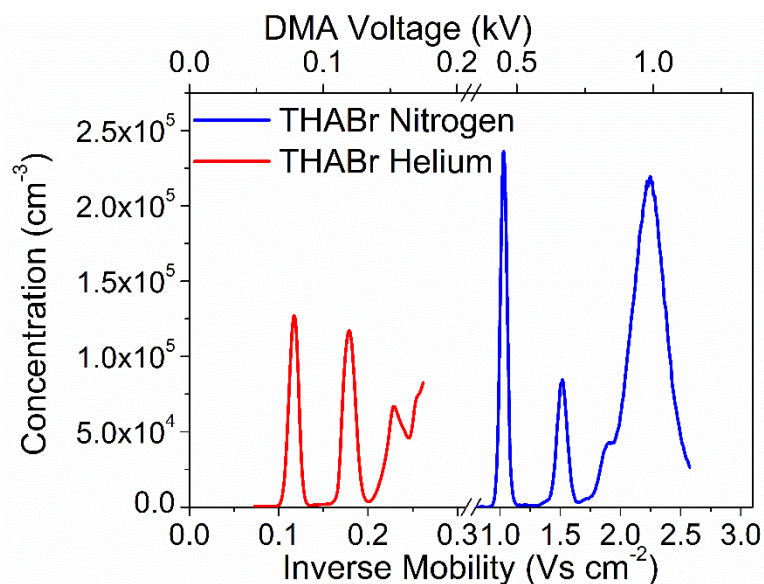
Figure 2. Comparison of inverse mobility distribution of THABr$^+$ electrosprayed and measured in helium and nitrogen. The top x-axis shows the voltage applied to the DMA, the bottom x-axis shows the inverse mobility.

4.3 Results and Discussion

Silver Cluster – Identification of cluster sizes through mobility measurements

The majority of mobility measurements of atomic clusters reported in the literature have been made with drift tubes, typically in tandem with mass spectrometry (MS). In these instruments the clusters are separated from each other by their drift times at a low pressure helium environment, and the absolute cluster sizes (number of atoms) are determined by MS (Furche et al. 2002; Gilb et al. 2002). Measuring the mobility of silver clusters in helium at atmospheric pressure in our measurements gives the opportunity for direct comparison with literature values. (Weis et al. 2002).
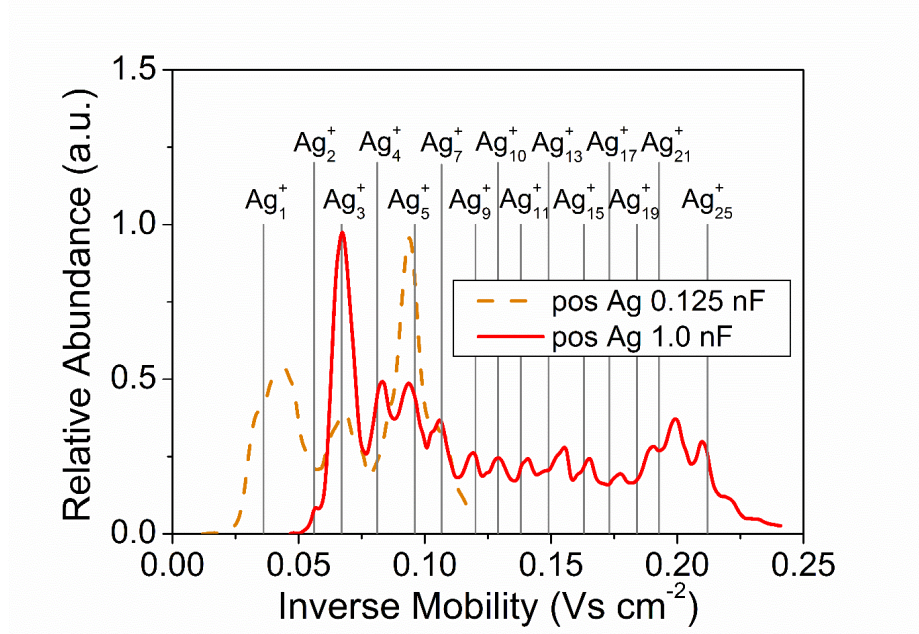
Figure 3. Inverse mobility distributions of positively charged atomic silver clusters generated and measured in purified helium. Vertical lines indicate the inverse mobilities of Ag clusters calculated based on experimental of collision cross sections reported in the literature (Weis et al. 2002).

Figures 3 and 4 show the measured inverse mobility distributions of positively and negatively charged silver atomic clusters, generated in purified helium gas, for two different values of spark energy, respectively. To facilitate comparison, the peaks were normalized to the highest concentration peak. Relative abundance is then determined as the ratio of the measured concentration over the concentration of the highest peak. The mean size of the clusters produced at lower spark energies (i.e., using a lower capacitance; cf. Eq. 1) are smaller compared to those at higher spark energies. Higher spark energies produce higher initial concentration of atoms and this leads to larger cluster sizes due to increased coagulation rate.

The labeled vertical lines in the distribution of the positively charged clusters (cf. Figure 3) are taken from collision cross sections reported in the literature (Gilb et al. 2002; Weis et al. 2002). The collision cross sections Ω were converted into inverse mobilities using:

$$\Omega = \frac{3ne}{16N_0} \sqrt{\frac{2\pi}{\mu k_B T}} \frac{1}{Z_0}, \qquad (3)$$

where N_0 is the number density of the gas, μ is the reduced mass of the ion and gas molecule, k_B is the Boltzmann constant, T is the absolute temperature; n is the number of elementary charges the cluster carries, which is equal to unity in our case. Because collision cross sections for negatively charged clusters are not available in the literature, the vertical lines in Figure 4 indicate the peaks of our measurements.
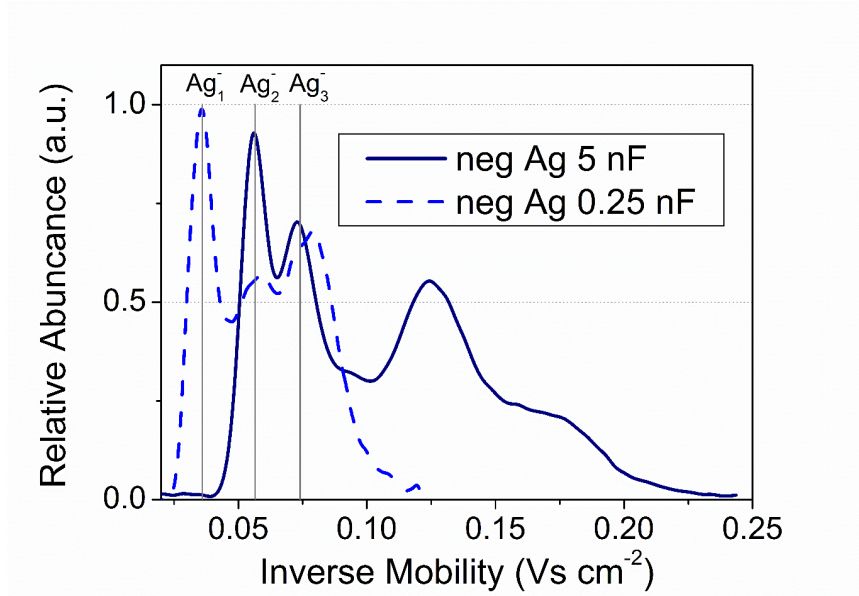

Figure 4. Inverse mobility distributions of negatively charged atomic silver clusters generated and measured in purified helium. The vertical lines indicate the inverse mobilities of the clusters measured in this work.

The first peak of the mobility distribution of the positively charged clusters, measured at 0.044 Vs cm^2 inverse mobility (equal to a collision cross section of 26 Å^2) is between the expected theoretical values for the one and two Ag atom cation. The shift of the first peak to a lower mobility compared to the theoretically expected value can be associated to the attractive ion-induced dipole interaction. The polarizability of the helium gas molecule leads to a potential that scales with $1/r^4$, where r is the distance between the point charge (ion) and the induced dipole (gas molecule). This means that the measured collision cross section for very small ions is governed mainly by the attractive interaction due to gas polarizability, rather than by the repulsive interaction due to collisions, which is determined by the van der Waals radii of the silver cluster and the He molecule (Gilb et al. 2002; Steiner et al. 2006; Tammet 1995). The shift in mobility for the first peak was also observed by Weis et al. (2002) who measured the first peak at 30.5 Å^2 (Z^{-1} =0.0523 Vs cm^2) while the calculated theoretically expected value was 20.8 Å^2 (Z^{-1} = 0.0357 Vs cm^2). The first peak in the mobility distribution of the negative clusters is observed at an inverse mobility of 0.0361 Vs cm^2 which is about 1 % higher than the theoretical value corresponding to the positively charged

peak (i.e. 0.0357 Vs cm^2). Although this deviation is within the uncertainty of our measurement, it can be explained by the difference in the size of the negative and positive clusters, due to the missing valence electron of the latter. The fact that the polarization effect is more significant for the smaller positive single atom than for the larger negative single atom can explain the measured difference in mobilities.

The observation of dominant peaks, corresponding to clusters consisting of odd number of atoms, in our measurements is consistent with cluster stability calculations available in literature (Peineke et al. 2009). Previous studies have shown that even-numbered neutral silver clusters show enhanced chemical stability due to electron pairing. Meanwhile, for charged clusters, electron pairing occurs when they consist of odd numbers of atoms (Bouwen et al. 1999; Peineke et al. 2009; Schmidt et al. 2003; Yannouleas and Landman 1995). Higher chemical stability leads to lower sensitivity to impurities and thus, more abundance in the measured distributions.

To check the validity of our measurements, Figure 5 shows a comparison between the collision cross sections derived from the mobility measurements of this study and those reported in the literature. The measured mobilities of silver cations in helium have, therefore, been converted to collision cross sections using Eq. 3. To account for pressure differences between our mobility measurements and the mobility measurements in Weis et al. (2002) both experimental values were converted to a reduced mobility Z_0 (expected mobility at 1 atm, and 273.15 K) using:

$$Z_0 = \frac{P}{P_0} \frac{273.15 \ [K]}{T} Z \ , \tag{4}$$

where P is the pressure in the measurement conditions, P_0 is the atmospheric pressure and T is the temperature during the experiment and Z is the measured mobility at the experimental pressure and temperature conditions (Clemmer and Jarrold 1997; Tammet 1995). In our measurements the pressure ranged from 1050 to 1160 mbar, whereas the temperature from 295 to 305 K, as measured with a pressure gauge (Series 902, MKS Inc.) and a thermocouple at the inlet of the DMA sheath flow.
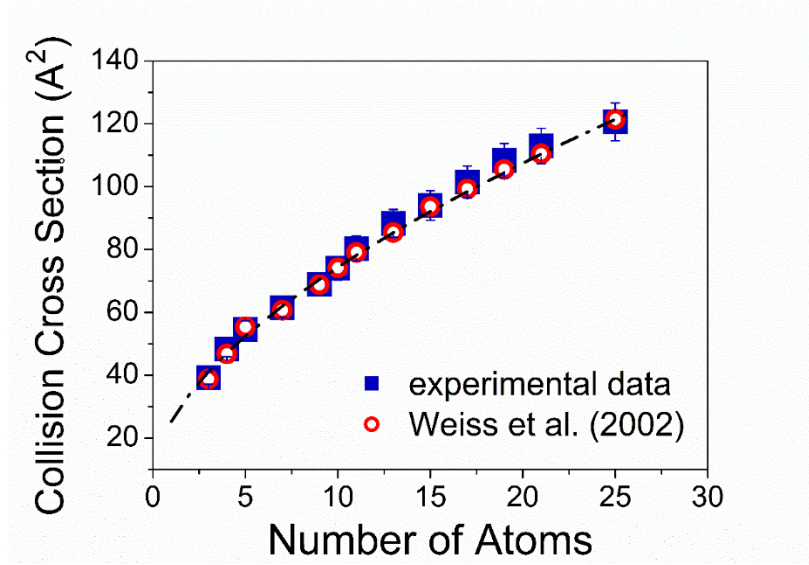
Figure 5. Comparison of collision cross sections (this work) with values from the measurements reported by Weis et al. (2002). The dash-dotted line is a fitted function to the experimental values provided by Weis et al. (2002) given by Eq. 5.

The dot-dashed line (cf. Figure 5) is a curve fitted to the experimental values of Weis et al. (2002) (i.e., same as in Figure 1 of Weis et al. (2002). The curve shows the increase of collision cross section with increasing number of atoms n of the cluster, which is given by:

$$\Omega(n) = \frac{4\pi}{3}\left(n^{\frac{1}{3}} \cdot r_{Ag} + r_{He}\right)^2, \tag{5}$$

where r_{Ag} and r_{He} are the radii of the silver atom and the helium molecule. In the fitting curve they are 1.52 and 0.94 Å, respectively.

The error bars in Figure 5 represent the uncertainty in our experimental results which was estimated to be within 5%, associated with the resolution of the DMA and small fluctuations in pressure and temperature during the measurements. The agreement between our experimental data and respective values reported in the literature is within experimental uncertainty for all data points, which verifies that the technique is suitable for generation of clusters.

Effect of Gas purity

An advantage of the SDG compared to other evaporation-condensation techniques is that the purity of the generated particles can only be affected by the purity of the electrode material and the purity of the gas. The two mobility distributions shown in Figure 6 correspond to positively

75

charged silver clusters, with and without purification of helium carrier gas. The measurements performed under non-purified conditions (red dashed line) exhibit two distinct peaks. In this case the carrier gas was used directly from the helium tank, which contains ppm levels of water and oxygen. The blue solid curve shows the mobility distribution measured at purified conditions with significantly lower water and oxygen levels compared to the non-purified case (ppb levels). Earlier studies have shown that water does not react with silver clusters in the absence of oxygen (Bréchignac et al. 1999a). As a result, the elimination of most peaks of the cluster mobility distribution can be attributed to etching by O_2. This is a well-known effect that has been verified using mass spectrometry (Leuchtner et al. 1989; Reber et al. 2007). It has been observed though that in the presence of oxygen, water reacts with the oxidized silver clusters (Bréchignac et al. 1999c).

The changes in the distributions are visible instantaneously, when switching to the purified gas line. This indicates that any effect of impurities on the generated clusters happens inside the spark chamber during or immediately after evaporation and not inside the classification zone of the DMA. The sheath gas adapts to the input purity slower than the time scale of a mobility measurement and the observed fast change indicates that contaminants in the sheath gas have no detectable influence.

The reaction of O_2 with clusters leads to the emission of atoms from clusters, and the emitted species react with instable clusters until they reach stable sizes. This explains why the stable peaks appear to grow in intensity at the cost of unstable ones. Considering that the level of impurities from the helium tank is in the ppm range, and can be reduced down to the ppb level by using the purification units, the mean collision rate of atomic clusters with oxygen molecules at atmospheric pressure can be reduced by three orders of magnitude (i.e., from 10^4 to 10^1 collisions/s).

In Figure 6 two dominant peaks are observed in the mobility distributions measured with non-purified helium. According to the comparison of literature values of ion mobility to our mobility measurements, the first peak is identified as the 3-atom (Ag_3^+) cluster (Weis et al. 2002). This corresponds to the magic numbers of electrons inside the clusters which can be related to shell closing (Brack 1993). The second dominant peak appears between the expected mobilities for Ag_7^+ and Ag_9^+. The Ag_9^+ peak should show enhanced stability because of the eight valence electrons in the cluster according to the Jellium model (Brack 1993). However, our measurements show that enhanced stability occurs closer to the Ag_7^+ cluster. It is known that rather stable bonds of silver with one or two oxygen atoms can be found at small cluster sizes (Schmidt et al. 2003). We assume

that this peak shows overlapping signals from various cluster species that cannot be resolved from one another. The possible configurations are Ag_7, Ag_7O, Ag_7O_2, and Ag_9 (Jackschath et al. 1992; Schmidt et al. 2003; Weis et al. 2002).
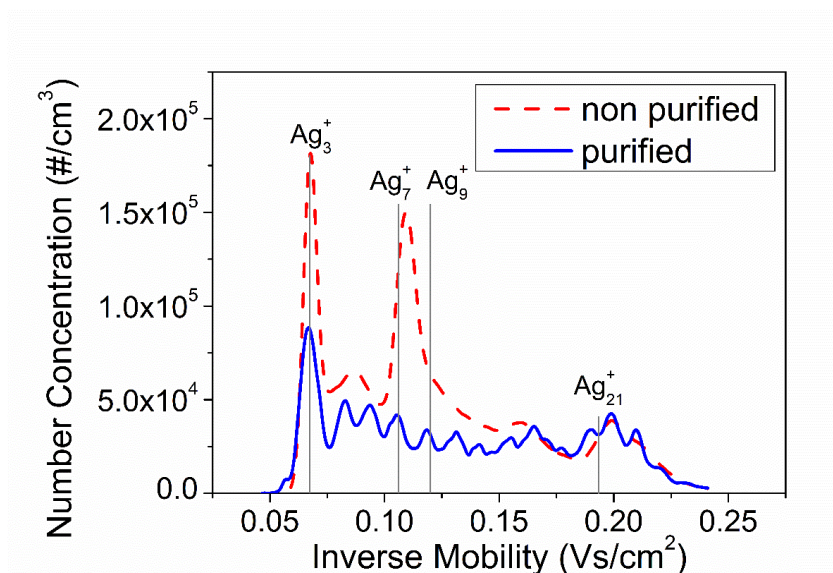

Figure 6. Comparison of mobility distributions of positively charged Ag clusters measured in purified (solid (blue) line) and non-purified (dashed (red) line) helium.

Our measurements also show that the Ag_{21}^+ clusters, which can also be associated to a magic number, exhibit enhanced stability. To identify the reactions of the Ag clusters with O_2, our mobility measurements would need to be combined with measurements of mass spectra. In addition, the resolving power of our ion mobility measurement is likely to be a limiting parameter in our measurements as it is not sufficient for a clear resolution of structural differences of different clusters. However, the goal of this study was to show that SDG can be used as a source of atomic clusters and the mobility measurements confirms the feasibility of the method.

4.4 Conclusions

In this work we demonstrated how spark ablation under atmospheric pressure is useful for synthesizing atomic clusters that range from 1 to 25 atoms in size. The produced clusters are either neutral or self (singly) charged (positively or negatively). The cluster sizes produced can be controlled by the spark energy. The method is capable of producing clusters of controlled purity. The impurity level in the gas flow affects the generated cluster distributions. At higher impurity levels stable clusters (magic numbers) dominate the produced distribution, and we attribute this to

oxidation etching. Thus, etching by oxidation can be intentionally applied in cases where higher concentrations of stable clusters are needed. The SDG method in combination with a DMA is an appropriate technique to generate and size select atomic clusters under atmospheric conditions.

The SDG has obvious advantages compared to other, more established, methods of cluster generation. The production, as well as size selection at atmospheric pressure, offers the opportunity of collecting virtually all of the generated material for application purposes. Furthermore, spark ablation does not require a vacuum pumping system and is thus a more energy efficient and cost-effective method than low-pressure systems.

Acknowledgements

References

Attoui, M., Paragano, M., Cuevas, J., Fernandez de la Mora, J. (2013). Tandem DMA Generation of Strictly Monomobile 1–3.5 nm Particle Standards. Aerosol Science and Technology 47:499-511.

Bondybey, V. and English, J. (1982). Laser excitation spectra and lifetimes of Pb2 and Sn2 produced by YAG laser vaporization. The Journal of Chemical Physics 76:2165-2170.

Bouwen, W., Vanhoutte, F., Despa, F., Bouckaert, S., Neukermans, S., Theil Kuhn, L., Weidele, H., Lievens, P., Silverans, R. E. (1999). Stability effects of Au n X m+(X= Cu, Al, Y, In) clusters. Chemical physics letters 314:227-233.

Brack, M. (1993). The physics of simple metal clusters: self-consistent jellium model and semiclassical approaches. Reviews of Modern Physics 65:677-732.

Bréchignac, C., Cahuzac, P., Leygnier, J., Tigneres, I. (1999a). Comparison of reactive nucleation of silver and alkali clusters in the presence of oxygen and water. The European Physical Journal D-Atomic, Molecular, Optical and Plasma Physics 9:421-424.

Bréchignac, C., Cahuzac, P., Leygnier, J., Tigneres, I. (1999b). Reactive nucleation of silver clusters with oxygen and water. Chemical physics letters 303:304-310.

Brus, D., Hyvärinen, A.-P., Ždímal, V., Lihavainen, H. (2005). Homogeneous nucleation rate measurements of 1-butanol in helium: A comparative study of a thermal diffusion cloud

chamber and a laminar flow diffusion chamber. The Journal of chemical physics 122:214506.

Chen, D., Pui, D. Y., Hummes, D., Fissan, H., Quant, F., Sem, G. (1996). Nanometer differential mobility analyzer (Nano-DMA): design and numerical modeling. Journal of Aerosol Science 27:137-138.

Cho, K., Wang, X., Nie, S., Shin, D. M. (2008). Therapeutic nanoparticles for drug delivery in cancer. Clinical cancer research 14:1310-1316.

Claridge, S. A., Castleman Jr, A., Khanna, S. N., Murray, C. B., Sen, A., Weiss, P. S. (2009). Cluster-assembled materials. Acs Nano 3:244-255.

Clemmer, D. E. and Jarrold, M. F. (1997). Ion mobility measurements and their applications to clusters and biomolecules. Journal of Mass Spectrometry 32:577-592.

de Heer, W. A. (1993). The physics of simple metal clusters: experimental aspects and simple models. Reviews of Modern Physics 65:611-676.

De Juan, L. and Fernández de la Mora, J. (1998). High resolution size analysis of nanoparticles and ions: Running a Vienna DMA of near optimal length at Reynolds numbers up to 5000. Journal of aerosol science 29:617-626.

de la Mora, J. F. and Kozlowski, J. (2013). Hand-held differential mobility analyzers of high resolution for 1–30nm particles: Design and fabrication considerations. Journal of Aerosol Science 57:45-53.

Dotan, I. and Albritton, D. (1977). Mobilities of F−, Cl−, Br−, and I− ions in argon. The Journal of Chemical Physics 66:5238-5240.

Fang, J., Wang, Y., Attoui, M., Chadha, T. S., Ray, J. R., Wang, W.-N., Jun, Y.-S., Biswas, P. (2014). Measurement of Sub-2 nm Clusters of Pristine and Composite Metal Oxides during Nanomaterial Synthesis in Flame Aerosol Reactors. Analytical chemistry 86:7523-7529.

Fernández, E. M., Soler, J. M., Garzón, I. L., Balbás, L. C. (2004). Trends in the structure and bonding of noble metal clusters. Physical Review B 70:165403.

Fuchs, N. (1963). On the stationary charge distribution on aerosol particles in a bipolar ionic atmosphere. Geofisica pura e applicata 56:185-193.

Furche, F., Ahlrichs, R., Weis, P., Jacob, C., Gilb, S., Bierweiler, T., Kappes, M. M. (2002). The structures of small gold cluster anions as determined by a combination of ion mobility measurements and density functional calculations. The Journal of chemical physics 117:6982-6990.

Gilb, S., Weis, P., Furche, F., Ahlrichs, R., Kappes, M. M. (2002). Structures of small gold cluster cations (Au+ n, n< 14): ion mobility measurements versus density functional calculations. The Journal of chemical physics 116:4094-4101.

Han, K., Kim, W., Yu, J., Lee, J., Lee, H., Woo, C. G., Choi, M. (2012). A study of pin-to-plate type spark discharge generator for producing unagglomerated nanoaerosols. Journal of Aerosol Science 52:80-88.

Hewitt, G. (1957). The charging of small particles for electrostatic precipitation. American Institute of Electrical Engineers, Part I: Communication and Electronics, Transactions of the 76:300-306.

Jackschath, C., Rabin, I., Schulze, W. (1992). Electron impact ionization of silver clusters Ag n, n≦ 36. Zeitschrift für Physik D Atoms, Molecules and Clusters 22:517-520.

Jena, P. (2013). Beyond the Periodic Table of Elements: The Role of Superatoms. The Journal of Physical Chemistry Letters 4:1432-1442.

Khanna, S. N. and Jena, P. (1995). Atomic clusters: Building blocks for a class of solids. Physical Review B 51:13705.

Knutson, E. and Whitby, K. (1975). Aerosol classification by electric mobility: apparatus, theory, and applications. Journal of Aerosol Science 6:443-451.

Kruis, F. E., Fissan, H., Peled, A. (1998). Synthesis of nanoparticles in the gas phase for electronic, optical and magnetic applications—a review. Journal of Aerosol Science 29:511-535.

Kulmala, M., Vehkamäki, H., Petäjä, T., Dal Maso, M., Lauri, A., Kerminen, V.-M., Birmili, W., McMurry, P. H. (2004). Formation and growth rates of ultrafine atmospheric particles: a review of observations. Journal of Aerosol Science 35:143-176.

Larriba-Andaluz, C., Fernández-García, J., Ewing, M. A., Hogan, C. J., Clemmer, D. E. (2015). Gas molecule scattering & ion mobility measurements for organic macro-ions in He versus N 2 environments. Physical Chemistry Chemical Physics 17:15019-15029.

Leite, E., Weber, I., Longo, E., Varela, J. A. (2000). A new method to control particle size and particle size distribution of SnO2 nanoparticles for gas sensor applications. Advanced Materials 12:965-968.

Leuchtner, R., Harms, A., Castleman Jr, A. (1989). Thermal metal cluster anion reactions: Behavior of aluminum clusters with oxygen. The Journal of chemical physics 91:2753-2754.

Luo, X., Morrin, A., Killard, A. J., Smyth, M. R. (2006). Application of nanoparticles in electrochemical sensors and biosensors. Electroanalysis 18:319-326.

Maißer, A., Premnath, V., Ghosh, A., Nguyen, T. A., Attoui, M., Hogan, C. J. (2011). Determination of gas phase protein ion densities via ion mobility analysis with charge reduction. Physical Chemistry Chemical Physics 13:21630-21641.

Martinez-Lozano, P., Labowsky, M., Fernández de la Mora, J. (2006). Experimental tests of a nano-DMA with no voltage change between aerosol inlet and outlet slits. Journal of aerosol science 37:1629-1642.

Meuller, B. O., Messing, M. E., Engberg, D. L., Jansson, A. M., Johansson, L. I., Norlén, S. M., Tureson, N., Deppert, K. (2012). Review of spark discharge generators for production of nanoparticle aerosols. Aerosol Science and Technology 46:1256-1270.

Moini, M. and Eyler, J. R. (1988). Formation of small negative and positive cluster ions of gold, silver, and copper by direct laser vaporization. The Journal of chemical physics 88:5512-5515.

Peineke, C., Attoui, M., Robles, R., Reber, A., Khanna, S., Schmidt-Ott, A. (2009). Production of equal sized atomic clusters by a hot wire. Journal of Aerosol Science 40:423-430.

Perelshtein, I., Applerot, G., Perkas, N., Guibert, G., Mikhailov, S., Gedanken, A. (2008). Sonochemical coating of silver nanoparticles on textile fabrics (nylon, polyester and cotton) and their antibacterial activity. Nanotechnology 19:245705.

Pratsinis, S. E. (1998). Flame aerosol synthesis of ceramic powders. Progress in Energy and Combustion Science 24:197-219.

Reber, A. C., Khanna, S. N., Roach, P. J., Woodward, W. H., Castleman, A. W. (2007). Spin accommodation and reactivity of aluminum based clusters with O2. Journal of the American Chemical Society 129:16098-16101.

Reischl, G. (1991). Measurement of ambient aerosols by the differential mobility analyzer method: concepts and realization criteria for the size range between 2 and 500 nm. Aerosol Science and Technology 14:5-24.

Rosser, S. and De La Mora, J. F. (2005). Vienna-type DMA of high resolution and high flow rate. Aerosol Science and Technology 39:1191-1200.

Scheibel, H. (1983). Generation of monodisperse Ag-and NaCl-aerosols with particle diameters between 2 and 300 nm. Journal of Aerosol Science 14:113-126.

Schmidt, M., Cahuzac, P., Bréchignac, C., Cheng, H.-P. (2003). The stability of free and oxidized silver clusters. The Journal of chemical physics 118:10956-10962.

Schwyn, S., Garwin, E., Schmidt-Ott, A. (1988). Aerosol generation by spark discharge. Journal of Aerosol Science 19:639-642.

Steiner, G., Attoui, M., Wimmer, D., Reischl, G. (2010). A medium flow, high-resolution Vienna DMA running in recirculating mode. Aerosol Science and Technology 44:308-315.

Steiner, W. E., English, W. A., Hill, H. H. (2006). Ion-neutral potential models in atmospheric pressure ion mobility time-of-flight mass spectrometry IM (tof) MS. The Journal of Physical Chemistry A 110:1836-1844.

Subramanian, V., Wolf, E., Kamat, P. V. (2001). Semiconductor-metal composite nanostructures. To what extent do metal nanoparticles improve the photocatalytic activity of TiO2 films? The Journal of Physical Chemistry B 105:11439-11446.

Tabrizi, N. S., Ullmann, M., Vons, V., Lafont, U., Schmidt-Ott, A. (2009). Generation of nanoparticles by spark discharge. Journal of Nanoparticle Research 11:315-332.

Tammet, H. (1995). Size and mobility of nanometer particles, clusters and ions. Journal of Aerosol Science 26:459-475.

Ude, S. and De la Mora, J. F. (2005). Molecular monodisperse mobility and mass standards from electrosprays of tetra-alkyl ammonium halides. Journal of aerosol science 36:1224-1237.

Ullmann, M., Friedlander, S. K., Schmidt-Ott, A. (2002). Nanoparticle formation by laser ablation. J Nanopart Res 4:499-509.

Vons, V. A. (2010). Spark discharge generated nanoparticles for hydrogen storage applications. PhD thesis, Delft University of Technology, Delft, The Netherlands.

Wang, L., Khalizov, A. F., Zheng, J., Xu, W., Ma, Y., Lal, V., Zhang, R. (2010). Atmospheric nanoparticles formed from heterogeneous reactions of organics. Nature Geoscience 3:238-242.

Wang, Y., Fang, J., Attoui, M., Chadha, T. S., Wang, W.-N., Biswas, P. (2014). Application of Half Mini DMA for sub 2nm particle size distribution measurement in an electrospray and a flame aerosol reactor. Journal of Aerosol Science 71:52-64.

Weis, P., Bierweiler, T., Gilb, S., Kappes, M. M. (2002). Structures of small silver cluster cations (Ag_n^+, n <12): ion mobility measurements versus density functional and MP2 calculations. Chemical physics letters 355:355-364.

Whitby, K. T. and Clark, W. E. (1966). Electric aerosol particle counting and size distribution measuring system for the 0.015 to 1 μ size range1. Tellus 18:573-586.

Wiedensohler, A. (1988). An approximation of the bipolar charge distribution for particles in the submicron size range. Journal of Aerosol Science 19:387-389.

Yannouleas, C. and Landman, U. (1995). Electronic shell effects in triaxially deformed metal clusters: A systematic interpretation of experimental observations. Physical Review B 51:1902-1917.

Zhang, Y., Shuiqing, L., Deng, S., Yao, Q., Stephen, D. T. (2012). Direct synthesis of nanostructured TiO 2 films with controlled morphologies by stagnation swirl flames. Journal of Aerosol Science 44:71-82.

Chapter 5

Size-dependent sign preference in ion-induced nucleation

Abstract

It is generally believed that nucleation of vapor molecules on gas ions has a unique preference towards a specific ion polarity; a phenomenon referred to as the sign preference. Water vapor for instance, has a preference to nucleate on negative ions as has originally been demonstrated by the pioneering experiments of C. T. R. Wilson in the late 1800s and corroborated by numerous studies thereafter. All the experimental evidence in support of the sign preference reported thus far, however, employ positive and negative ions of different species. As a result, understanding whether the sign preference is solely due to the sign or the structure/composition of the ions is still elusive. In this work spark ablation was used, as a method to generate positive and negative silver ions that in principle have the same composition but different sizes (i.e., the number of atoms they contain), and expose them to supersaturated atmospheres of vapour molecules. Contrary to what is believed so far, results show that the sign preference is not unique, but it can alternate for a given pair of molecule-ionic species. This alternating behavior depends on the number of atoms forming the ion, thus on its electronic structure, and not only on the ionic charge sign. Experimental data shows that this behavior holds both for polar and non-polar vapor molecules, although for the latter it is less pronounced.

5.1 Introduction

Ion-induced nucleation has been a field of high scientific interest for many decades due to its importance in atmospheric processes. Ions in the atmospheric environment form efficient nuclei on which inorganic and organic vapors can condense, thereby yielding high concentrations of newly-formed airborne nanoparticles.[1-5] Particles formed by ion-induced nucleation in the atmosphere can further grow by condensation and/or coagulation, and thus affect the visibility and the climate of the Earth in a direct manner.[6,7] In addition, particles produced by ion-induced nucleation can act as cloud condensation nuclei when exposed to supersaturated conditions of water vapors. [8,9]

Ion-induced nucleation of water vapors has been extensively studied since the pioneering experiments of C. T. R. Wilson.[10] In fact, Wilson was the first to report that water vapors nucleate more efficiently on negative compared to positive ions. This effect has since then been referred to as the sign preference. Apart from water, the same (i.e., negative ion) sign preferences has also been reported for n-propanol.[11] In contrast, other vapor molecules (e.g., dibutylphthalate, methanol and acetonitrile) have been shown to exhibit a nucleation preference towards positive molecules.[12-15] All these studies demonstrate that the preference of specific vapor molecules to nucleate on negative or positive ions depends strongly on the composition of the molecules.

More recently, Kangasluoma et al. showed that apart from the nucleating vapor, a key parameter defining ion-induced nucleation is the chemical composition of the ion.[16] They demonstrated that by measuring the nucleation probability of three different liquids on positively, negatively and neutral sub-3 nm particles. Their work strengthens the consensus that sign preference is rather specific to the seed ion-liquid chemical interactions.

Sign preference has also been investigated by several modelling studies.[23-26] A common conclusion amongst these studies is that the key to understanding the phenomenon lies in the electronic structure of the ions. Nadykto *et al*. have shown that this electrostatic interaction is stronger with decreasing size of the ion and that by accounting for their electronic structure, good agreement between experiments and theory can be achieved.[25-26] To validate the model predictions and further understand the underlying mechanisms of ion-induced nucleation, however, we need experimental observations involving ions of well-defined electronic structure and chemical composition.

In this chapter, we report novel experimental observations of ion-induced nucleation aiming to understand the effect of the sign preference beyond the current state of the art. In contrast to previous studies where the size, structure and composition of ions was not taken into account, here we employ ions consisting of 2 up to 22 atoms. The novelty in those observations is in the ability to produce positive and negative ions of different size, starting from that of a single atom, that in principle are of the same chemical composition. Butanol and nonane were chosen as representatives of polar and non-polar molecules, respectively, to study the preference of nucleation on either positive or negative ions.

5.2 Experimental Procedure

Details of the generation method of the silver ions (referred to as ionic clusters from this point onwards) used in this study are provided in a previous publication of our group.[17] In brief, a Spark Discharge Generator (SDG)[18] was used to ablate silver in order to generate ionic clusters suspended in high-purity He or N_2 gas. The SDG produces ions of variable sizes, the majority of which carry a single positive or negative elementary charge. To select ionic clusters of one polarity having sizes within a very narrow range (i.e., monodisperse ions) we used a high-resolution Differential Mobility Analyzer (DMA; SEADM Model half-mini)[19] downstream the SDG. Upon exiting the DMA, the concentration of the monodisperse ionic clusters was measured in parallel by a Condensation Particle Counter (CPC; TSI Model 3025),[20] in which we could control the supersaturation level, and a custom-made Faraday cage electrometer (EM).

The CPC consists of a heated saturator in which a working fluid (butanol or nonane in our case) evaporates and saturates the sample flow, and of a condenser that provides a controlled region of supersaturated vapor by subsequently cooling the sample flow. Ionic clusters that enter the supersaturated region act as nucleation sites for the vapors of the working fluid, resulting in the formation of droplets that are subsequently counted by an optical detector inside the CPC. It should be noted here that the ionic clusters cannot be directly detected (i.e., without growing to micron-sized droplets) by the optical detector, and thus the CPC can only measure the concentration of the ions that have effectively acted as nucleation sites for the vapors.

The concentration of the droplets formed in the CPC is always a fraction of the total concentration of the sampled ions that depends on the size of the ions, the condensing vapor, and the operating conditions. As a result, the ions can be detected by the CPC with a specific efficiency. To determine the detection efficiency of the CPC during the measurements, a constant fraction of the flow entering the CPC is branched off into the EM, which determines the ion current trapped in the Faraday cage. The detection efficiency, which is proportional to the nucleation efficiency of the ions when passed through the CPC, was then calculated as the ratio of the CPC signal over the signal of the EM. For a specific value of the supersaturation in the supersaturated region of the CPC, the detection efficiency is directly related to the probability that an ion surpasses the energy barrier required for droplet formation, and therefore the nucleation efficiency.

5.3 Results and Conclusions

Figure 1 shows the mobility distribution of both positive and negative ionic clusters produced by the SDG in He. The spectra have peaks that correspond to ionic clusters containing 1 to 25 silver atoms. Evidently, the peaks are more pronounced in the mobility spectrum of the negative ions, reflecting their higher stability as has been systematically observed in previous studies.[21] The same experimental procedure was used to produce silver ionic clusters in N_2. The respective mobility distributions obtained in N_2 exhibit the same characteristics as the one in He (data not shown here).

It should be noted here that the mobility of the ionic silver clusters produced by the SDG is proportional to their ionic collision cross section and thus to their size. The number of silver atoms corresponding to each peak in the mobility distribution was estimated by calculating the associated cross sections and using the respective values (or relation) provided by Weis et al.[22] This analysis, along with detailed presentation of the experimental details are provided by Maisser *et al.*[17]
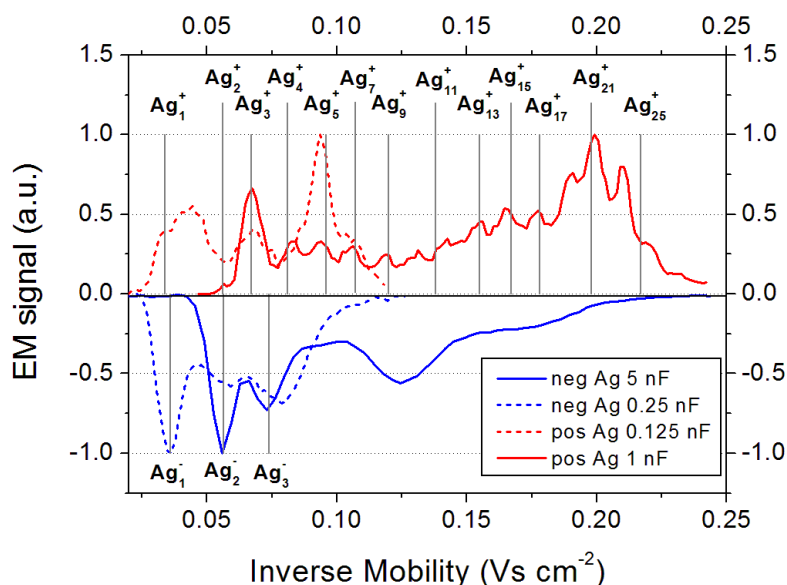

Figure 1. Measured mobility spectra of positive and negative silver ionic clusters produced by the SDG in He. The two spectra of ionic clusters for each polarity correspond to different operating conditions (i.e., capacitance of the electric circuit producing the sparks) of the SDG.

Figure 2 shows the measured nucleation efficiency of butanol on positive and negative ionic clusters suspended in N_2. The inverse mobility of 0.8 Vs/cm^2, corresponding to ionic clusters with 7 silver atoms, constitutes a threshold dividing their behaviour in two different regimes of sign preference. Positive ions appear to be more efficient nuclei when they contain up to ca. 7 silver atoms, whereas negative ions nucleate butanol vapors more effectively when they contain 7 to 10 atoms. For ions with inverse mobility larger than ca. 1.2 Vs/m^2 positive ions appear to be again more effective nuclei, with nucleation efficiency being higher than those of their negative counterparts. Evidently, the preference of butanol vapor molecules to nucleation on ionic clusters of Ag is not unique for one polarity, but it can switch from positive to negative depending on the size of the ionic clusters. To the best of our

knowledge, it is the first time that such an alternating sign preference has been observed experimentally for ionic clusters of the same chemical composition.

The crossover of the sign preference observed in this study is consistent with modelling results reported in literature. Oh *et al.* studied theoretically the nucleation of methanol vapor on ions and predicted a positive sign preference which they attribute to the competition between molecule-molecule interaction, ion-molecule electrostatic interaction and the orientation of the methyl group on the surface of the nucleating ion.[23] Their calculations show that a crossover behaviour of the sign preference is theoretically possible. Pointing at the same direction, Kathmann *et al.* calculated the chemical potential of small aqueous positive and negative ions and found that the relationship with size is nonmonotonic.[24] They found that with decreasing size, the chemical potentials can cross each other leading to a switch in sign preference.
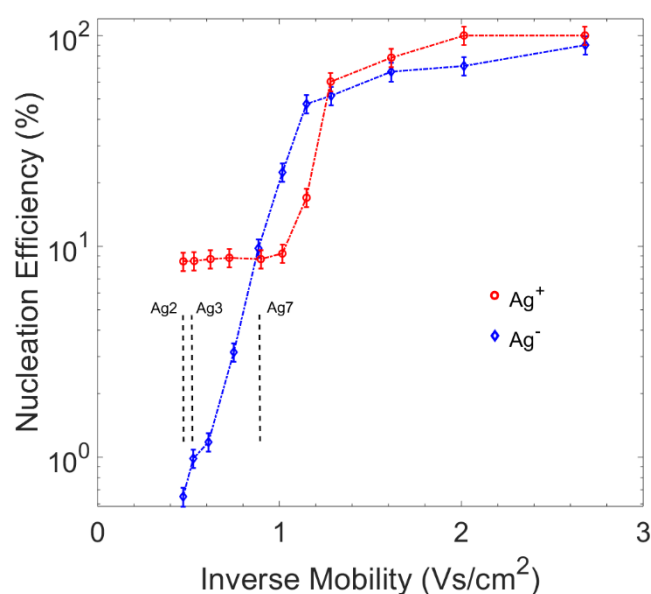

Figure 2. Measured nucleation efficiency of butanol on negative and positive silver ionic clusters in nitrogen.

To investigate the effect of vapor polarity on the nucleation efficiency, we performed the same experiments with nonane vapors. Nonane is a molecule with a small dipole moment (0.07 D) compared to butanol (1.66 D). As a result, nonane molecules are attracted towards the ionic clusters primarily by the induced dipole moment. Measurements of the nucleation efficiency of the non-polar molecule vapors (nonane) on both positive and negative ionic clusters are shown in Figure 3. Indeed, there are no significant differences of the nucleation efficiency of nonane between positive and negative ions above an inverse mobility of 0.15 Vs/cm^2, corresponding approximately to Ag_{12}. However, below Ag_{12}, a pronounced positive *sign preference* seems to exist. In the vicinity of the ion, the molecule becomes a dipole, and is therefore attracted to the ion. Results indicate that switching to a low dipole moment molecule, positive and negative ions exhibit approximately the same qualitative nucleation behaviour

with the one observed for higher dipole moment molecules: i.e., positive ionic clusters are more effective nuclei than negative when they contain up to a few atoms, whereas the sign preference is either switched or becomes comparable for larger ions. These results indicate that the molecules' dipole moment influence on the qualitative behaviour of nucleation is weak.
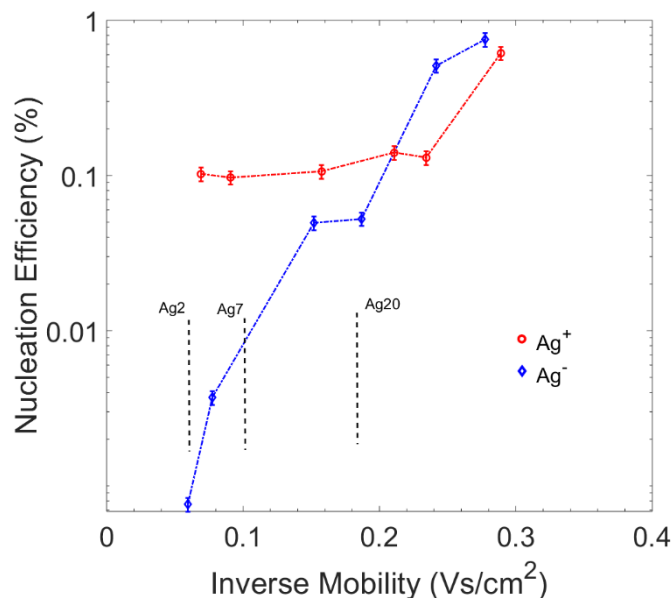

Figure 3. Measured nucleation efficiency of nonane on negative and positive silver atomic clusters in He.

An interesting observation in the data shown in Figs. 2 and 3 is the plateau corresponding to the smaller positive ions, suggesting that they are activated with the same efficiency, regardless of their size, by both polar and non-polar molecules. This can be understood by considering the thermodynamic aspect of nucleation. Vapor molecules attach to the ion to form a cluster ion with an equilibrium diameter defined by a local minimum of the Gibbs free energy as a function of cluster size. Any ion with diameter smaller than the equilibrium diameter corresponding to the energy local minimum will follow the thermodynamically favorable route to form the same stable cluster ion, yielding the same nucleation efficiency. Following this rationale, one would expect to observe a similar plateau for the case of the negative ions, since the formation of the stable cluster ion is independent of the charge sign. Our observations indicate that this is clearly not the case, as the measured nucleation efficiency on negative ions decreases with decreasing ionic size.

A possible explanation for this observation is the difference in the stability between Ag_n^+ and Ag_n^-. This can be understood by considering that metal atoms have a rather low electron affinity (1.3 eV for Ag). For electron emission into a dielectric liquid, the energy required may very well be only 1/10 of this energy[27], so that thermal emission of the negative charge becomes probable at room temperature. For clusters (n>1), the electron affinity, and therewith stability, increases. We speculate that upon

adsorption of the vapor, Ag_n^- is unstable for very small n. This explains the fundamentally different nucleation behavior of Ag_n^- and Ag_n^+, and that this is generalizable to all metal ions and all ions with a small enough electron affinity.

The purity of ions is a parameter that certainly can affect the nucleation behavior of vapors, especially when considering their small size. A first indication that the ionic clusters studies in this work behave similar to those in pure, vacuum-based studies is provided by the fact that they exhibit the odd-even peak oscillations that are expected for pure clusters. Parallel mass spectra of the ionic clusters would certainly have provided evidence of the purity of the ionic clusters, but that was not possible when the experiments were carried out. Our preliminary measurements on the composition of the silver ionic clusters produced by the SDG, however, indicate that pure silver ionic clusters can be produced, and that the most common impurities include trace amounts of water and oxygen that get through the purification system. The oxygen reactions that are enabled by water traces in the system make the chemical composition of the clusters for both polarities very similar as we found the presence of Ag+, AgOH+, AgOH2+, Ag2+, AgOH+, AgOH2+ for positive ions and Ag-, AgOH-, AgOH2-, Ag2-, Ag2OH-, Ag2O2H4- for negative ions.

This work shows the first experimental evidence that the sign preference for a specific ion-molecule pair can alternate between positive and negative ions. The experimental data demonstrate that the established paradigm, which states that every ion-molecule pair exhibits a unique sign preference, is invalid at least for the materials investigated in this study. The key factor enabling this study was the ability to use positive and negative clusters of the same material. The experimental data and the considerations presented in this work can be seen as in-line with former studies mentioned above, in so far as they conclude that chemistry plays a role in sign preference of nucleation. Even if the material is the same, Ag for both signs, positive and negative silver ions must be considered as chemically different.

References

[1] Kulmala, M., Science 302 (5647), 1000 (2003)

[2] Kulmala,M., Vehkamäki, H., Petäjä, T., Dal Maso, M., Lauri, A., Kerminen, V.M., Birmili,W., McMurry, P.H., J. Aerosol Sci. 35 (2), 143 (2004b)

[3] Kulmala,M., Petäjä, T., Nieminen, T., Sipilä,M., Manninen, H.E., Lehtipalo, K., DalMaso,M., Aalto, P.P., Junninen, H., Paasonen, P., Riipinen, I., Lehtinen, K.E.J., Laaksonen, A., Kerminen, V.M., Nat. Protoc. 7 (9), 1651 (2012)

[4] Kulmala, M., Kontkanen, J., Junninen, H., Lehtipalo, K., Manninen, H.E., Nieminen, T., Petäjä, T., Sipilä, M., Schobesberger, S., Rantala, P., Franchin, A., Jokinen, T., Järvinen, E., Äijälä, M., Kangasluoma, J., Hakala, J., Aalto, P.P., Paasonen, P., Mikkilä, J., Vanhanen, J., Aalto, J., Hakola, H., Makkonen, U., Ruuskanen, T., Mauldin III, R.L.,Duplissy, J., Vehkamäki, H., Bäck, J., Kortelainen, A., Riipinen, I., Kurtén, T., Johnston, M.V., Smith, J.N., Ehn, M., Mentel, T.F., Lehtinen, K.E.J., Laaksonen, A., Kerminen, V., Worsnop, D.R., Science 339 (6122), 943 (2013)

[5] Zhang, R., Khalizov, A.,Wang, L., Hu,M., Xu,W., Chem. Rev. 112 (3), 1957 (2012)

[6] Pöschl, U., Chem. Int. Ed. 44 (46), 7520 (2005)

[7] Yue, D., Hu,M.,Wu, Z.,Wang, Z., Guo, S.,Wehner, B., Nowak, A., Achtert, P.,Wiedensohler, A., Jung, J., Kim, Y., Liu, S.,. J. Geophys. Res. 114 (D2) (2009)

[8] Kulmala, M., Petäjä, T., Ehn, M., Thornton, J., Sipilä, M., Worsnop, D.R., Kerminen, V.M.,. Annu. Rev. Phys. Chem. 65, 21 (2014)

[9] Dusek, U., Frank, G.P., Curtius, J., Drewnick, F., Schneider, J., Kürten, A., Rose, D., Andreae, M.O., Borrmann, S., Pöschl, U., Geophys. Res. Lett. 37, 3 (2010).

[10] Wilson, C.T.R., Phil. Trans. R. Soc. A 189, 265 (1897)

[11] Winkler, P.M. et al. , Science, 319, 1374 (2008)

[12] Adachi, M.; Okuyama, K.; Seinfeld, J. H, J. Aerosol Sci., 23, 327 (1992)

[13] Seto, T.; Okuyama, K.; de Juan, L.; Fernández de la Mora, J, J. Chem. Phys., 107, 1576 (1997)

[14] Okuyama, K.; Adachi, M.; Shinagawa, H.; Shi, G.; Seinfeld, J. H. J. Aerosol Sci., 22, S85 (1991)

[15] Kane, D.; Daly, G. M.; Elshall, M. S. J. Phys. Chem., 99, 7867 (1995)

[16] Kangasluoma J., Samodurov A., Attoui M., Franchin A., Junninen H., Korhonen F., Kurtén T., Vehkamäki H., Sipilä M., Lehtipalo K., Worsnop D.R., Petäjä T., and Kulmala M., *J. Phys.* Chem. C, 120 (13), 7444 (2016)

[17] Maisser, A., Barmpounis, K.; Attoui, M. B.; Biskos, G.; Schmidt-Ott, A., Aer. Sci.Tech. 10, 886 (2016)

[18] Tabrizi, N. S., Ullmann, M., Vons, V., Lafont, U., and Schmidt-Ott, A., J. Nanopart. Res., 11:315 (2009)

[19] de Juan, L., and de la Mora, J. F. , J. Aerosol Sci., 29:617 (1998)

[20] Whitby, K. T., and Clark, W. E., Tellus, 18:573 (1966)

[21] Bernhardt,T.M.,J.Mass.Spec.,243,1 (2005)

[22] Weis,P. , Bierweiler,T. ,Gilb,S. ,Kappes,M.M. , Chem.Phys.Let., 355 (2002)

[23] Oh,K.J. , Gao,G.T. , Zeng, X.C., Phys.Rev.Let., 86,22 (2001)

[24] Kathmann,S.M. , Schenter,G.K., Garrett,B.C. , Phys.Rev.Let., 98, 116104 (2005)

[25] Nadykto,A.B.,Natsheh,A.A. , Yu,F. , Mikkelsen,K.V. , Ruuskanen,J., Phys.Rev.Let. , 96,125701 (2006)

[26] Nadykto, A.B. , Yu, F., J. Geoph. Res., 108, 4717 (2003)

[27] LePage, W.R., DuBridge, L. A., Phys. Rev., 58 (1940)

6. Conclusions and Summary

Understanding the processes related to particle formation in the atmosphere is crucial in order to quantify more accurately their effect on climate. New particle formation is a global scale phenomenon, through which significant amounts of new particles are introduced in the atmosphere. A main mechanism of new particle formation is ion-induced nucleation, where vapor molecules nucleate on pre-existing atmospheric ions. It follows that in order to understand the mechanism of ion-induced nucleation, research must be focused on the very first steps of formation which normally lay in the sub-2nm size range. The work of this thesis is focused on facilitating the research on new particle formation by advancing the instrumentation state-of-the-art, but also performing experimental work on the dynamics of ion-induced nucleation.

In **Chapter 2,** we introduce a new operation method of laminar flow condensation particle counters which greatly enhances their ability to detect sub-2nm particles. The main finding is that reducing the nucleation temperature leads to enhanced counting efficiencies. At the optimum operating temperatures, we measured a 40% increase in the detection efficiency for the smallest ion used in the study (0.94 nm). Good agreement of the experimental results with calculations deriving from the Kelvin-Thompson theory was found. In addition, simulations of the supersaturation profile inside the condenser tube revealed that the observed enhancement is attributed to the enlargement of the area which the supersaturation covers, followed by a slight increase of the supersaturation maximum value. Furthermore, we show that by choosing the right temperature window the supersaturation maximum can be defined with much greater resolution than any existing method can achieve. It is the first time that the concept of manipulating the spatial characteristic of the supersaturation profile is introduced in the operation of laminar flow CPCs. The fact that our method does not require any hardware modifications of the CPC, makes it extremely attractive and easy to apply. The number of laminar flow CPCs that are used in aerosol research is high, and therefore this method is highly relevant.

In **Chapter 3**, we describe a novel manufacturing concept which enables the production of low weight and low-cost Differential Mobility Analyzers (DMAs). This new concept relies on manufacturing a DMA out of plastic instead of metal, which has been used traditionally in the manufacturing process. The DMA is then coated with an electrically conductive layer, in order to acquire the conductivity necessary for the electric field. To test this method, two identical DMAs were built, one out of plastic and one out of stainless steel, and their performance was compared by measuring their transfer functions in a Tandem DMA configuration. Excellent agreement of the measured midpoint mobility diameters was found, with small deviations at high sheath flow rates. These deviations are attributed to expected non-idealities of the plastic DMA, which cause small disturbances of the sheath

flow field. The two main innovative characteristics of the new DMA are portability and low cost. The implications of this work are numerous, and its generality can be applied in other aerosol instruments, since electrically conductive surfaces is a key specification of all aerosol related equipment. The light-weight and low-cost DMAs pave the way to the development of an SMPS with the same characteristics. Making the SMPS widely accessible facilitates the expansion of monitoring station networks that are currently operating around the world. Furthermore, it enables their use in Unmanned Aerial Vehicles (UAVs) for measuring the vertical profiles of aerosol particles in the atmosphere. By using 3D-printing technology, our method enables aerosol scientists to manufacture their own DMAs. This means that modifications and improved designs can be easily made and tested, at a fraction of the cost that would be needed if the same DMAs were made of metal. More importantly, our method has great educational value since it offers graduate and PhD students the opportunity to design and produce their own instruments, without the bottleneck of extensive simulations and high cost related manufacturing processes.

In **Chapter 4,** we optimize the operation of a spark discharge generator (SDG) for the production well defined atomic clusters of high purity, which are the ideal seed particles for investigating ion-induced nucleation. The atomic clusters were made out of silver and contained a varying number of atoms ranging from 1 to 25. We show how by varying the amount of energy that is released with every spark, the size of clusters can be tuned. In addition, we show that by controlling the trace amounts of O_2 and H_2O present in the carrier gas, one can tune the production of cluster species with specific number of atoms (magic number). The SDG is a very attractive method due to its simple operation and low infrastructure demands. It operates at atmospheric pressure and thus it does not require high vacuum pump systems. This makes it a simple and yet highly stable and reliable atomic cluster generator that is ideal for nucleation studies.

Chapter 5 focuses on the investigation of the sign-preference dynamics in ion-induced nucleation. In order to eliminate the dependence of the nucleation on the chemical affinity between the ion and the vapor molecule, we used the SDG to produce negative and positive ions from the same material. Silver atomic clusters were used as ions, while butanol and nonane were used as nucleating vapors. Measurements of the nucleation probability of butanol vapors on positive and negative silver atomic clusters revealed an alternating sign-preference that has been observed experimentally for the first time.

Samenvatting

Het is van cruciaal belang om de processen die gerelateerd zijn aan deeltjesvorming in de atmosfeer te begrijpen om het effect ervan op het klimaat nauwkeurig te kunnen kwantificeren. Het vormen van nieuwe deeltjes is een fenomeen op wereldschaal, waardoor significante hoeveelheden nieuwe deeltjes in de atmosfeer geïntroduceerd worden. Een voornaam mechanisme voor het vormen van nieuwe deeltjes is door ionen geïnduceerde nucleatie, waarbij dampmoleculen een groeikern vormen op bestaande atmosferische ionen. Het volgt dat om het mechanisme van door ionen geïnduceerde nucleatie te begrijpen, onderzoek gericht moet worden op de allereerste stappen in het vormingsproces, welke normaliter in het sub-2nm deeltjesgroottebereik liggen. Het werk in dit proefschrift richt zich op het faciliteren van onderzoek naar het vormen van nieuwe deeltjes door de stand van de techniek van instrumentatie te verbeteren, maar ook door het uitvoeren van experimenteel werk op de dynamica van door ionen geïnduceerde nucleatie.

In **Hoofstuk 2**, wordt een nieuwe werkwijze voor laminar flow condensation particle counters (CPCs) geïntroduceerd, welke hun vermogen om sub-2nm deeltjes te detecteren sterk verbetert. De voornaamste bevinding is dat het verlagen van de nucleatietemperatuur leidt tot verhoogde efficiëntie van het tellen. Bij de optimale werktemperaturen maten wij een stijging van 40% in de detectie-efficiëntie van het kleinste ion in deze studie (0.94 nm). De experimentele resultaten komen goed overeen met berekeningen afgeleid van de Kelvin-Thompson theorie. Bovendien blijkt uit simulaties van het oververzadigingsprofiel in de condensatiebuis dat de geobserveerde verbetering toe te wijzen is aan het vergroten van het oppervlak dat door de oververzadiging wordt gedekt, gevolgd door een lichte verhoging van de maximale oververzadiging. Verder kan door het juiste temperatuurbereik te kiezen het maximum van de oververzadiging met veel grotere resolutie bepaald worden dan met bestaande methodes mogelijk is. Dit is de eerste keer dat het concept van het manipuleren van de spatiale karakteristiek van het oververzadigingsprofiel in CPCs met laminaire stroming is geïntroduceerd. Het feit dat deze methode geen wijzigingen in de hardware van de CPC vereist, maakt deze zeer aantrekkelijk en gemakkelijk om toe te passen. In het gebied van aerosolonderzoek is een groot aantal laminar flow CPCs in gebruik, zodat deze methode zeer relevant is.

In **Hoofdstuk 3** wordt een nieuw fabricatieconcept gepresenteerd, welke het vervaardigen van lichtgewicht en goedkope Differential Mobility Analyzers (DMAs) mogelijk maakt. In dit nieuwe concept wordt gekozen om de DMA uit plastic te vervaardigen, in plaats van uit metaal zoals traditionele vervaardigingsprocessen wordt toegepast. Vervolgens wordt de DMA bekleed met een elektrisch geleidende laag, om zo de voor het elektrisch veld benodigde geleidbaarheid te verkrijgen. Om deze methode te testen zijn er twee identieke DMA's gebouwd, één uit plastic en één uit roestvast

staal, en zijn de prestaties daarvan vergeleken door hun transferfunctie te meten in Tandem DMA configuratie. Er is een uitstekende overeenkomst gevonden tussen de gemeten midpunt mobiliteitsdiameter, met kleine afwijkingen bij hoge stroomsnelheid van het mantelgas. Deze afwijkingen worden toegewezen aan verwachtte non-idealiteit van de plastic DMA, welke kleine verstoringen in het stromingsveld van het mantelgas veroorzaken. De twee voornaamste innovatieve karakteristieken van deze nieuwe DMA zijn draagbaarheid en prijs. De implicaties van di twerk zijn talrijk, en kan generiek worden toegepast in andere aerosolinstrumenten, gezien elektrisch geleidende oppervlakken een belangrijke specificatie zijn voor alle aan aerosolen gerelateerde apparatuur. De lichtgewicht en goedkope DMA's maken het mogelijk om een SMPS te ontwikkelen met dezelfde karakteristieken. Door de SMPS, een instrument dat een centrale rol speelt in aerosolonderzoek, toegankelijk te maken wordt het uitbreiden van de netwerken van meetstations die wereldwijd actief zijn vergemakkelijkt. Verder maakt dit het mogelijk om deze instrumenten in Unmanned Aerial Vehicles (UAVs) te gebruiken voor het meten van de verticale profielen van aerosoldeeltjes in de atmosfeer. Door het toepassen van 3D-printtechnologie maakt deze methode het mogelijk voor aerosolonderzoekers om hun eigen DMA's te fabriceren. Dit betekent dat modificaties en verbeterde ontwerpen gemakkelijk gemaakt en getest kunnen worden, tegen een fractie van de kosten welke gemaakt worden wanneer dezelfde DMA's uit metaal worden gemaakt. Belangrijker is dat deze methode grote educatieve waarde heeft aangezien dit studenten en aio's de kans biedt om hun eigen instrumenten te ontwerpen en te ontwikkelen, zonder de horde van uitgebreide simulaties of hoge kosten van de benodigde fabricageprocessen.

Hoofdstuk 4 gaat over het optimaliseren van de werking van een vonkgenerator (spark discharge generator, SDG) voor het maken van chemisch goed-gedefinieerde atomaire clusters van hoge zuiverheid, welke de ideale nucleatiekernen zijn voor het bestuderen van door ionen geïnduceerde nucleatie. De atomaire clusters zijn gemaakt van zilver, en bestonden uit een variërend aantal van 1 tot 25 atomen. Er wordt aangetoond hoe de grootte van de clusters gestuurd kan worden door de hoeveelheid energie die vrijkomt bij elke vonk te variëren. Bovendien kan men, door de hoeveelheid van O_2 en H_2O die als sporen in het draaggas aanwezig zijn te controleren, het vormen van clustersoorten met specifieke aantallen atomen (magic numbers) sturen. De SDG is een zeer aantrekkelijke methode door de simpele bediening en lage vereisten aan infrastructuur. Ze werkt bij atmosferische druk, en heeft derhalve geen hoogvacuum pompsystemen nodig. Dit maakt de SDG een simpele en desondanks zeer stabiele en betrouwbare generator voor atomaire clusters die ideaal is voor nucleatiestudies.

Hoofdstuk 5 richt zich op het bestuderen van de dynamiek van polariteitsvoorkeur bij door ionen-geïnduceerde nucleatie. Om de afhankelijkheid van nucleatie van de chemische affiniteit tussen het ion en de dampmolecule te elimineren, is de SDG gebruikt om negatieve en positieve ionen van hetzelfde

materiaal te maken. Voor nucleatie zijn dampen van butanol en nonaan gebruikt. Metingen van de nucleatiekans van butanoldamp op positieve en negatieve atomaire clusters van zilver onthullen een alternerende polariteitsvoorkeur welke voor het eerst experimenteel is geobserveerd.

Acknowledgements

Publications

- K. Barmpounis[*], A. Ranjithkumar, A. Schmidt-Ott, M. Attoui, G.Biskos, *Enhancing the Detection Efficiency of Condensation Particle Counters for Sub-2 nm Particles,* Journal of Aerosol Science, 117, 44-53, 2018

- K. Barmpounis[*], A. Maisser, A. Schmidt-Ott, G. Biskos, *Lightweight Differential Mobility Analyzers: Toward New and Inexpensive Manufacturing Methods*, Aerosol Science and Technology, 50:1, ii-v, 2016

- A. Maißer[1], K. Barmpounis[1], M. Attoui, G. Biskos, A. Schmidt-Ott, *Atomic Cluster Generation with an Atmospheric Pressure Spark Discharge Generator*, Aerosol Science and Technology, 49, 886-894, 2015

- K. Barmpounis[*], A. Maißer, M. Attoui, G. Biskos, A. Schmidt-Ott, *Experimental Observation of Sign Preferenced Ion-induced Nucleation of polar and non-polar molecules,* (in preparation)

- K. Barmpounis[*], A. Ranjithkumar, A. Schmidt-Ott, G.Biskos, *Pulse-Height Analysis with an Unmodified Monochromatic Condensation Particle Counter,* (in preparation)

- N.C. Surawski, S.Bezantakos, K.Barmpounis, M. C. Dallaston, A.Schmidt-Ott, G.Biskos, *A tunable high-pass Filter for Simple and Inexpensive Size-segregation of sub-10-nm Nanoparticles,* Nature Scientific Reports, 7, 45678, 2017

- S. Bezantakos, L. Huang, K. Barmpounis, S.T. Martin, G. Biskos, *Relative humidity non-uniformities in Hygroscopic Tandem Differential Mobility Analyzer Measurements,* Journal of Aerosol Science, 101, 1-9, 2016

- S. Bezantakos, L. Huang, K. Barmpounis, M. Attoui, A. Schmidt-Ott & G. Biskos , *A Cost-Effective Electrostatic Precipitator for Aerosol Nanoparticle Segregation*, Aerosol Science and Technology, 49:1, iv-vi, 2015

- S. Bezantakos, K. Barmpounis, M. Giamarelou, E. Bossioli, M. Tombrou, N. Mihalopoulos, K. Eleftheriadis, J. Kalogiros, J.D. Allan, A. Bacak, C.J. Percival, H. Coe, G. Biskos, *Chemical composition and hygroscopic properties of aerosol particles over the Aegean Sea*, Atmos. Chem. Phys., 13, 11595-11608, 2013

---

[1] Equal contribution of K. Barmpounis and A.Maisser
[*]corresponding author

Curriculum Vitae

Personal Information

Date of Birth: 03/03/1982

Nationality: Greek

Email: k.barmpounis@lemonlabs.eu

Education

Ph.D. Candidate in Nanotechnology (2012 – 2020)
Chemical Engineering Department, Technical University of Delft, The Netherlands

M.Sc. Environmental and Ecological Engineering (2009)
University of the Aegean, Dept. of the Environment, Mytilene, Greece

B.Sc. Physics (2008), Department of Physics, University of Patras, Patra, Greece

Dissertations

M.Sc. Thesis (2009)   *Bipolar Diffusion Charging: Experimental and Theoretical Evaluation of the Parameters Affecting the Charge Distribution of Nanoparticles in the Size Range of 10-100 nm.*
University of the Aegean, Dept. of the Environment, Mytilene, Greece
Supervisor: Prof. George Biskos

BSc. Thesis (2008)   *Non-linear Time Series Analysis in Atmospheric Physics.*
Department of Physics, University of Patras, Patra, Greece
Supervisor: Prof. Athanasios Argyriou

Professional Appointments

Postdoctoral Researcher (2019-Present), Max Planck Institute for Chemistry, Mainz, Germany

Lemon Labs Ltd (2016-present), Founder

- Lemon Labs is a start-up company developing portable, cost-effective instruments for nanoparticle detection and characterization, based on patented technology.

Research Assistant (2015-2017), EEWRC, The Cyprus Institute, Nicosia, Cyprus.

- Developer of the newly formed Aerosol Instrumentation Laboratory.
- Aerosol instrument development, characterization and adaptation to Unmanned Aerial Vehicles.

Researcher (Pre-doc) (2012-2015), Dept. of Chemical Engineering, TU Delft, Delft, The Netherlands

- Development of Portable Instrument for Monitoring Health Relevant Properties of Nanoparticles.

Research Interests

- Nanoparticle Mobility Analysis Instrumentation
- Ion-induced Nucleation
- Nano-engineered Atomic Clusters (sub-2 nm particles)
- Dynamics of Nanoparticle Formation
- Gas Phase Properties of Nanoparticles

Patents

- Lightweight Particle Mobility Analyzers, Patent Application Nr. 500132105, The Netherlands, 2015